8973-10-P

REMOTE SENSING TECHNIQUES FOR THE LOCATION AND MEASUREMENT OF SHALLOW-WATER FEATURES

F. C. POLCYN
R. A. ROLLIN

January 1969

Infrared and Optical Sensor Laboratory
Willow Run Laboratories
INSTITUTE OF SCIENCE AND TECHNOLOGY
THE UNIVERSITY OF MICHIGAN
Ann Arbor, Michigan

ensn

UMR1132

FOREWORD

This report is one of a series in a program to develop new remote sensing techniques and to demonstrate their feasibility in a variety of earth-resources applications. The general goal of this program is to develop methods of improving and extending current airborne and spaceborne survey capabilities; improvements are sought in the kinds and quantity of data obtainable and in the quality and economy of data interpretation. The program was initiated and is being guided by M. R. Holter, Head of the Infrared and Optical Sensor Laboratory of Willow Run Laboratories, a unit of The University of Michigan's Institute of Science and Technology.

This report was prepared under Contract N62306-67-C-0243 for the Spacecraft Oceanography Project, U. S. Naval Oceanographic Office. It is the first annual report under this contract, covering the period July 1967 through September 1968. The Principal Investigator for the research is D. S. Lowe, Head of the Sensory Systems Group of the Infrared and Optical Sensor Laboratory. Contributions to this report were made by

F. Polcyn, Project Leader
R. Rollin, Laser Systems Study
H. Burge, Algal Distribution Study
V. Noble and C. Huang, Wave-Refraction Study
J. Cook, Thermal Anomaly Study
W. Brown, Optical-Mechanical Scanner Systems Tradeoff Studies

ABSTRACT

The use of satellites with remote sensors to aid in the location of shallow waters or other obstructions to navigation over large areas in a relatively short time is being considered. The observables upon which the remote sensors will operate are color, time difference of reflected laser signals, and water-wave refraction; use of thermal anomalies for location information was considered but appears to hold little promise for depth determination. Laser ranging techniques for direct measurement of water depth have been analyzed, and sensor specifications have been derived. The attractiveness of systems employed for wave-refraction detection is enhanced through the use of two-dimensional optical processing techniques to aid in the sorting of data for determination of wavelength changes. The use of multispectral data (in the visible region) collected by cameras and/or optical-mechanical scanners was investigated for the condition where signal return (or film density) correlates with water depth. System parameters for optical-mechanical scanners have been derived for different values of bottom reflectance and attenuation of light in water. A survey of the literature on algae depth distribution was made to determine whether depth of water can be inferred from knowledge of the species present.

CONTENTS

FIGURES

TABLES

REMOTE SENSING TECHNIQUES FOR THE LOCATION AND MEASUREMENT OF SHALLOW – WATER FEATURES

First Annual Report
July 1967 Through September 1968

1
INTRODUCTION AND SUMMARY

The need for updating navigation charts to remove doubtful hydrographic data was expressed as a major concern at the Fourth Session of the International Oceanographic Committee meeting in 1965. The use of satellites with remote sensors has been considered under the present contract as a technique which may aid in the location of shallow waters or other obstructions to navigation over large areas in a relatively short time. To gain an understanding of the magnitude of the problem, consider the number and distribution of doubtful soundings for the North Atlantic Ocean as reported in reference 1; figure 1 is extracted from that report.

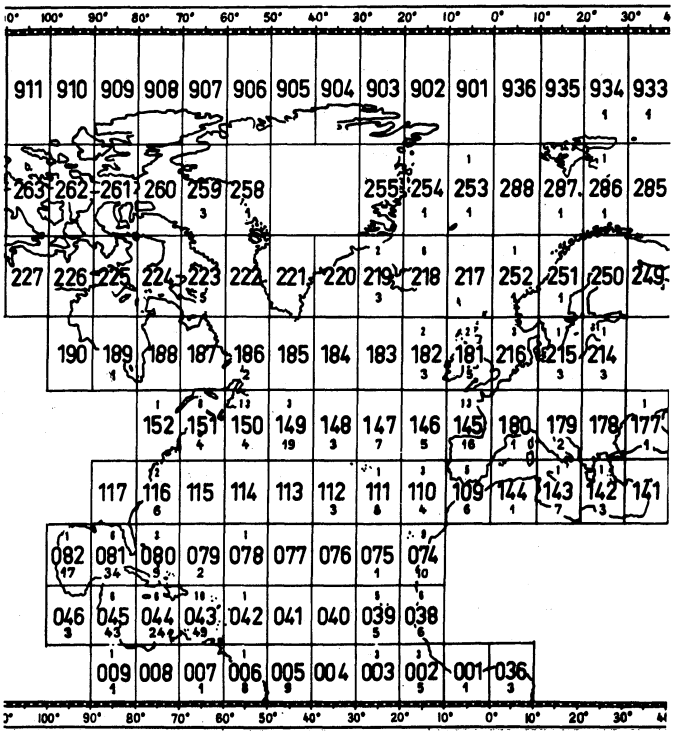

FIGURE 1. NUMBER AND DISTRIBUTION OF DOUBTFUL SOUNDINGS FOR THE NORTH ATLANTIC OCEAN [1]

Note that in Marsden square 043, there are listed 49 doubtful soundings and 10 other soundings for which doubt has been removed. Many doubtful soundings have been due to errors brought about in the use of the lead line in collecting the data or in the use of the echo sounder by operators of small fishing boats. The lead line usually measures too great a depth, because of the curving of the line. The echo sounder usually measures too shallow a depth, because soundings may result from intermediate scattering layers and because small-boat operators do not use their sounders continuously, with the result that the proper range scale may be in doubt. Often the error is in location and is due to inexact knowledge of the ship's position. If satellite technology is to be of any help, there must be consistent observables which the sensors can detect for location information; once a detection is made, the accuracy of the geographical position will depend on knowledge of the satellite's position and altitude in orbit. Figure 2 shows the relationships among several factors of importance in the determination of water depth.

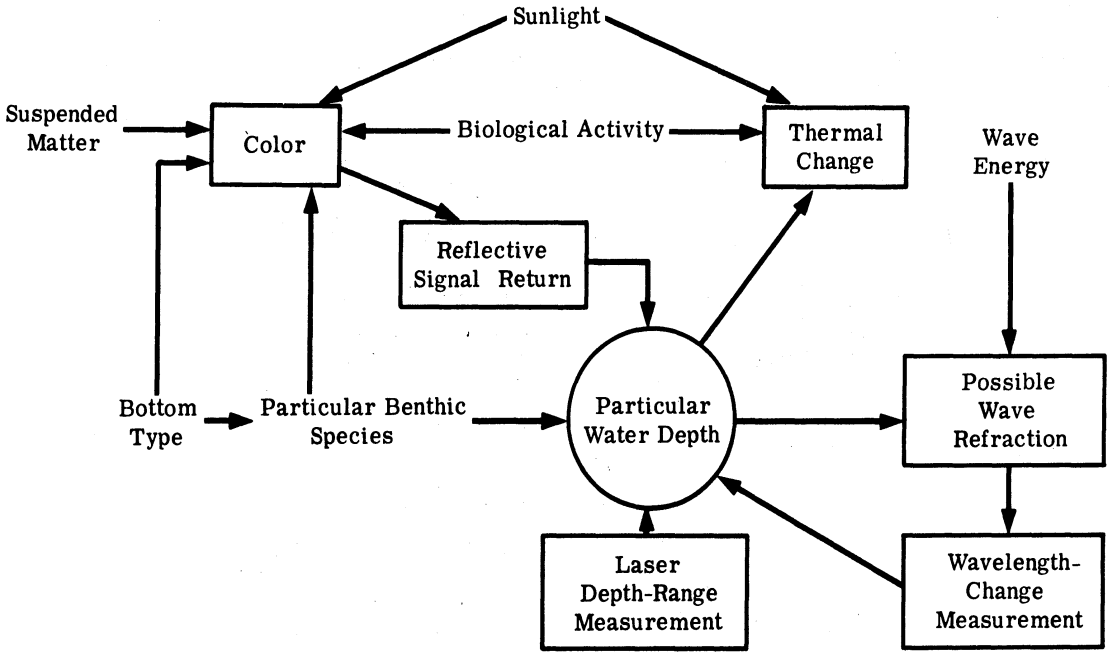

FIGURE 2. RELATIONSHIPS AMONG OBSERVABLES INDICATING CHANGE IN WATER DEPTH

Color and thermal change, wave refraction, and laser signal return (time difference) are the observables upon which a remote sensor will operate. As in all detection problems, the final classification of a particular depth will depend on a "convergence of evidence" from several sensors, because each one by itself may not be wholly reliable, and false detections

may be encountered from time to time. The reliability of color anomaly as an indicator of depth is influenced by the spectral quality of the sunlight, by suspended material, by bottom material type, and by the algal species present; it can be expected, though, that shallow areas will be greener and will, under certain conditions, produce water-wave refraction. If feasible laser systems can be built, direct measurement of water depth by laser ranging is a possibility. Thermal anomaly holds the least promise because it is not specifically related to water depth; it is well known that thermal differences can be observed at the surface, but it is difficult to reliably interpret the differences as related to shallow water rather than to some other factor. (In special cases, however, thermal anomaly is related to shoal formation caused by volcanic activity.) Table I lists the types of sensors that may be employed from spacecraft or aircraft to remotely detect the effects associated with shallow water. Consideration of cost, size, ease of processing, all-weather capability, etc., must be included in the final selection of sensors for operational use.

TABLE I. SENSORS THAT MAY BE USED FOR DETECTION OF OBSERVABLES ASSOCIATED WITH SHALLOW WATERS

Observable	Sensor
Color, density	Camera Optical-mechanical scanner (multispectral) TV system
Thermal anomaly	Optical-mechanical scanner Radiometer
Wave refraction	Camera, TV, optical-mechanical scanner Radar Laser imager
Time difference of reflected laser signals	Laser depth ranger

In section 2, the results of a survey on transmission of electromagnetic radiation in coastal water in comparison to deep ocean water are reported. In the assessment of sensor systems—i.e., photographic systems, optical-mechanical scanners, TV, and lasers—the amount of light loss in the water layer above the submerged feature, as well as the wavelength of the light for best penetration, are of crucial importance. In section 3, the potential of algal growth and distribution as an aid to determining water depth is discussed. Section 4 is concerned with the role of multispectral sensing in the mapping of features by their spectral signatures and in its potential for measuring depth using two or more channels of information. Section 5 gives the results of an investigation of water-wave refraction as a potential indicator of depth which

should be of particular significance for those areas where light penetration of water is poor. Section 6 is a short discussion of the potential of thermal anomalies as indicators of shallow water. Section 7 is a discussion of the feasibility of laser depth-ranging systems operating from aircraft or spacecraft platforms; a comparison of laser system sizes and specifications for aircraft and spacecraft sensors is also presented.

2
TRANSMISSION OF ELECTROMAGNETIC RADIATION IN COASTAL WATERS

Optimal photography of objects under water surfaces and use of laser ranging systems to measure the depth of submarine features require an intimate knowledge of the spectral transmittance of pure, ocean, and coastal waters, and of the effects of inorganic and organic particles on these transmittances. Water is a denser optical medium than air, and electromagnetic waves (natural sunlight, sky light, or monochromatic laser radiation) are refracted at the surface of the water according to the well-known refraction principle of Snell's Law (see fig. 3):

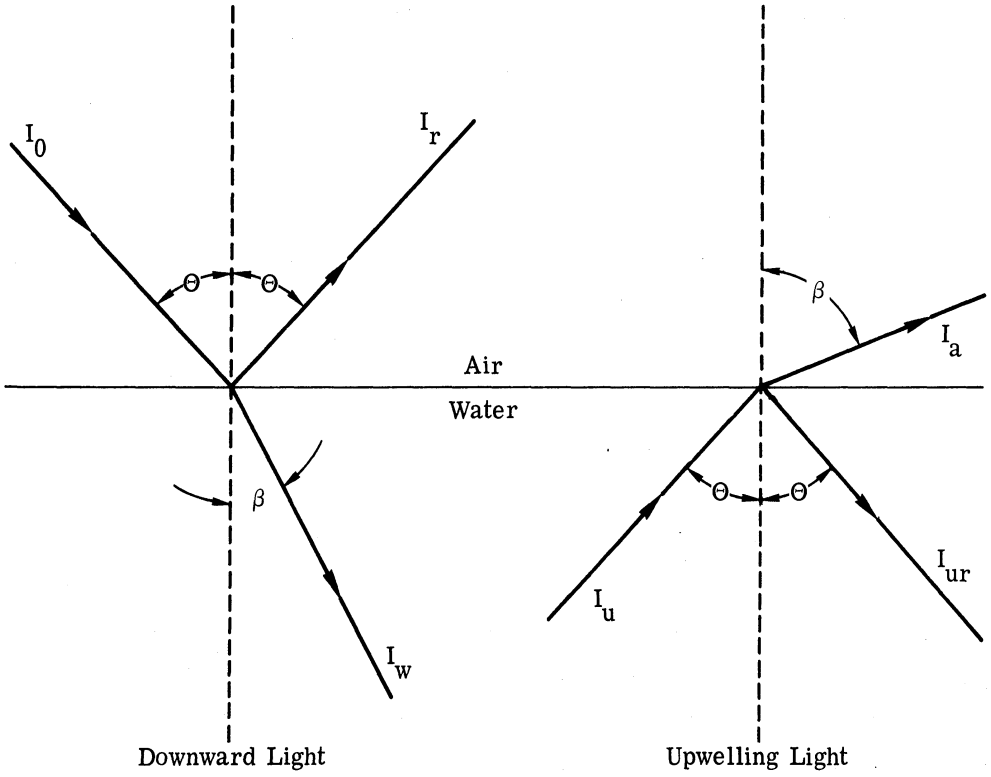

FIGURE 3. GEOMETRY FOR SNELL'S LAW. r = reflected component, u = upwelling component.

$$\frac{\sin \theta}{\sin \beta} = \frac{c_a}{c_w} = n_{w\text{-}a} \qquad (1)$$

where a, w = air, water

θ = angle of incidence from the normal

β = angle of transmission from the normal

c_a = velocity of light in air (299,793 ± 0.3 km/sec)

c_w = velocity of light in water

$n_{w\text{-}a}$ = relative index of refraction of water = 1.33335 at 20°C and λ = 0.5893 μ [3].*

All the radiant intensities (I) shown in figure 3 are scattered and absorbed by water according to Beer's Law:

$$I_z = I_0 e^{-\alpha z}$$

where I_z = intensity after traveling a distance z

I_0 = intensity at the surface

z = distance traversed in the water

α = total attenuation coefficient, or extinction coefficient, with units of reciprocal length

and $\alpha = \alpha_s + \alpha_a$

where α_s = scattering coefficient of the medium and its suspended particles

α_a = absorption coefficient

Both the scattering and the absorption coefficient are wavelength dependent (or frequency dependent). The attenuation coefficient (α) of air in an ARDC (Air Force Research and Development Command) model atmosphere at a wavelength of 0.5 μ at sea level is 1.84 (10^{-4}) m^{-1}, but for pure water, α is 2.36 (10^{-2}) m^{-1} at its maximum transparency wavelength, 0.47 to 0.48 μ [4, 5]; for pure water, α_s is 0.0086 and α_a is 0.015. The absorption coefficient of filtered sea water varies widely with frequency and wavelength, as shown in figure 4. (This curve was composed from Naval Research Laboratory (NRL) data for the spectrum 10^3 to 10^{13} Hz [6] and from data in reference 7, which were greatly smoothed for the 0.3- to 30-μ region.) Note from figure 5 that the maximum and the minimum attenuation (both α_a and α_s) occur at 3 μ and 0.47 μ, respectively. Figure 5 is a detailed portion of figure 4 showing attenuation coefficient vs. wavelength for the 0.1- to 10-μ region [7, 8]. There is some smoothing in figure 5 but not as much as in figure 4.

*The index of refraction varies in the third decimal place with temperature, wavelength, salinity, and concentration of suspended particles; sea water, having a temperature of 20°C and salinity of 35%, has an $n_{w\text{-}a}$ of 1.3339995 [4].

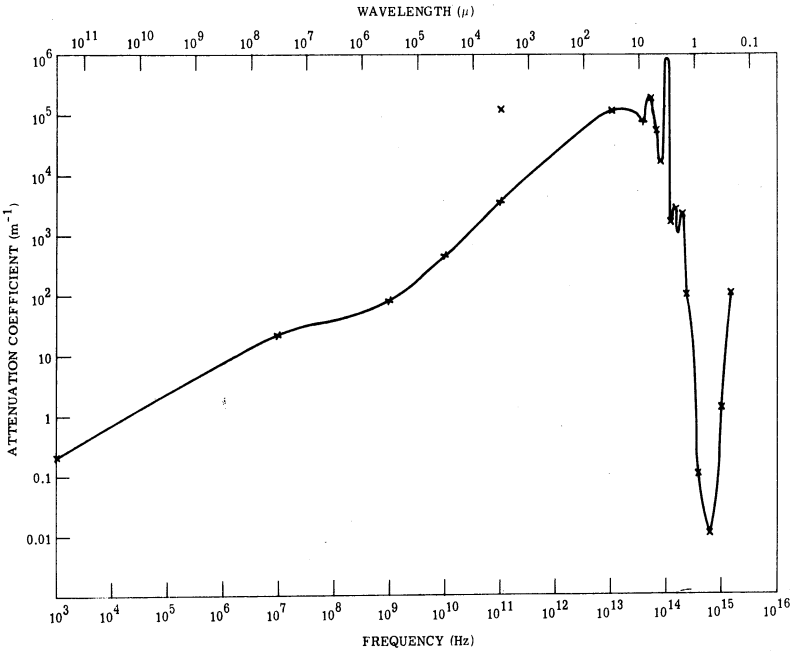

FIGURE 4. ATTENUATION COEFFICIENT VERSUS WAVELENGTH AND FREQUENCY FOR SEA WATER

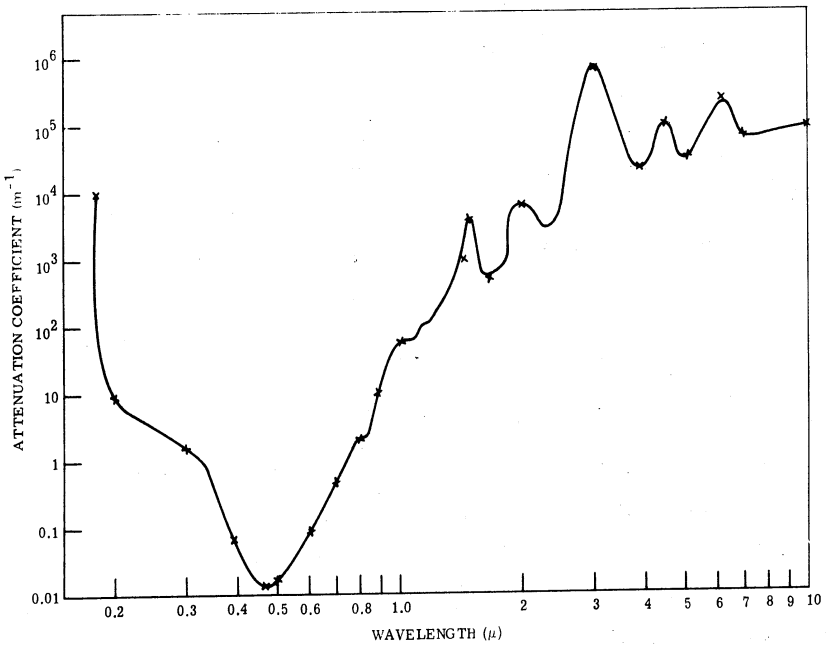

FIGURE 5. ATTENUATION COEFFICIENT VERSUS WAVELENGTH (ULTRAVIOLET, VISIBLE, AND INFRARED) FOR SEA WATER

The greatest discrepancies in attenuation-coefficient values are found in the 0.1- to 0.3-μ and 0.6- to 0.7-μ regions for both pure water and filtered sea water. Measurements give the total attenuation coefficient, but the scattering coefficient for distilled water and filtered sea water must be computed by scattering theory, with the remaining portion being the absorption coefficient. Figure 6 gives the ratio of the scattering coefficient to the absorption coefficient for filtered sea water and distilled water as determined by LeGrand [8]. Note that α_s is always less than α_a, except between 0.444 and 0.473 μ for distilled water and well-filtered sea water. α_s increases by 1 order of magnitude with the shorter wavelengths and is greatest in the 0.36- to 0.505-μ region. Thus, the scattering of solar radiation by water molecules causes very clear sea water and lake water to appear bluish, but coastal water, bays, and rivers tend to be greenish and yellowish because larger particles (>0.5 μ in diameter) are suspended in the water. Besides changing the color of the water, suspended particles shift the maximum-transmittance wavelengths toward longer wavelengths. Table II lists the wavlengths of maximum transmittance for various ocean waters and for pure water [9, 10]. The figures are essentially the same for pure water and the clearest ocean water.

Figure 7 compares the spectral attenuation coefficients for various coastal waters and pure water with measurements taken at nine geographical locations by two research teams as given in table III [11, 12]. The curve for pure water in figure 7 is composed of data taken by Utterback [13] for the 0.46- to 0.56-μ region and by Collins [14] for the 0.56- to 0.70-μ region. The curve for distilled water is composed of data taken by Utterback [13] for the 0.46- to 0.50-μ region and by Sullivan [15] for the 0.56- to 0.70-μ region. Since the curves for pure and distilled water cross at 0.673 μ, this may indicate an error in one or both of the measurements. The Sullivan measurements used the Nielson spectrometer with a resolution of 0.1 to 5 mμ with a given reproducibility of ± 2 (10^{-4}). The Collins measurements (made in 1939) used an instrument with a much lower resolution. The lower visible and ultraviolet portion (>0.46 μ) of the curve for pure water is from data taken by Sawyer in 1931 [9]. The three curves for coastal water and the mean oceanic curve for sea water are from Utterback's data [13]. As indicated in table III and figure 7, the minimum attenuation coefficients (maximum sea water transmittance) of the mean ocean and coastal waters off the coast of the state of Washington shift toward longer wavelengths, the "maximum coastal" curve having its minimum at 0.549 μ. According to the data of Utterback, the clearest ocean water has an attenuation coefficient of only twice that of pure water for the visible spectrum, but in figure 7, the mean attenuation coefficients for ocean water are 4 to 5 times that of pure water. As shown in figure 7, for the 0.46- to 0.60-μ region, minimum, mean, and maximum attenuation coefficients of coastal waters are, respectively, 16, 24, and 30 times that of pure water. Points A thru H for coastal waters (table III) all lie between the mean ocean curve and the maximum coastal curve in figure 7. The difference in the transmittance of ocean water and coastal water is due

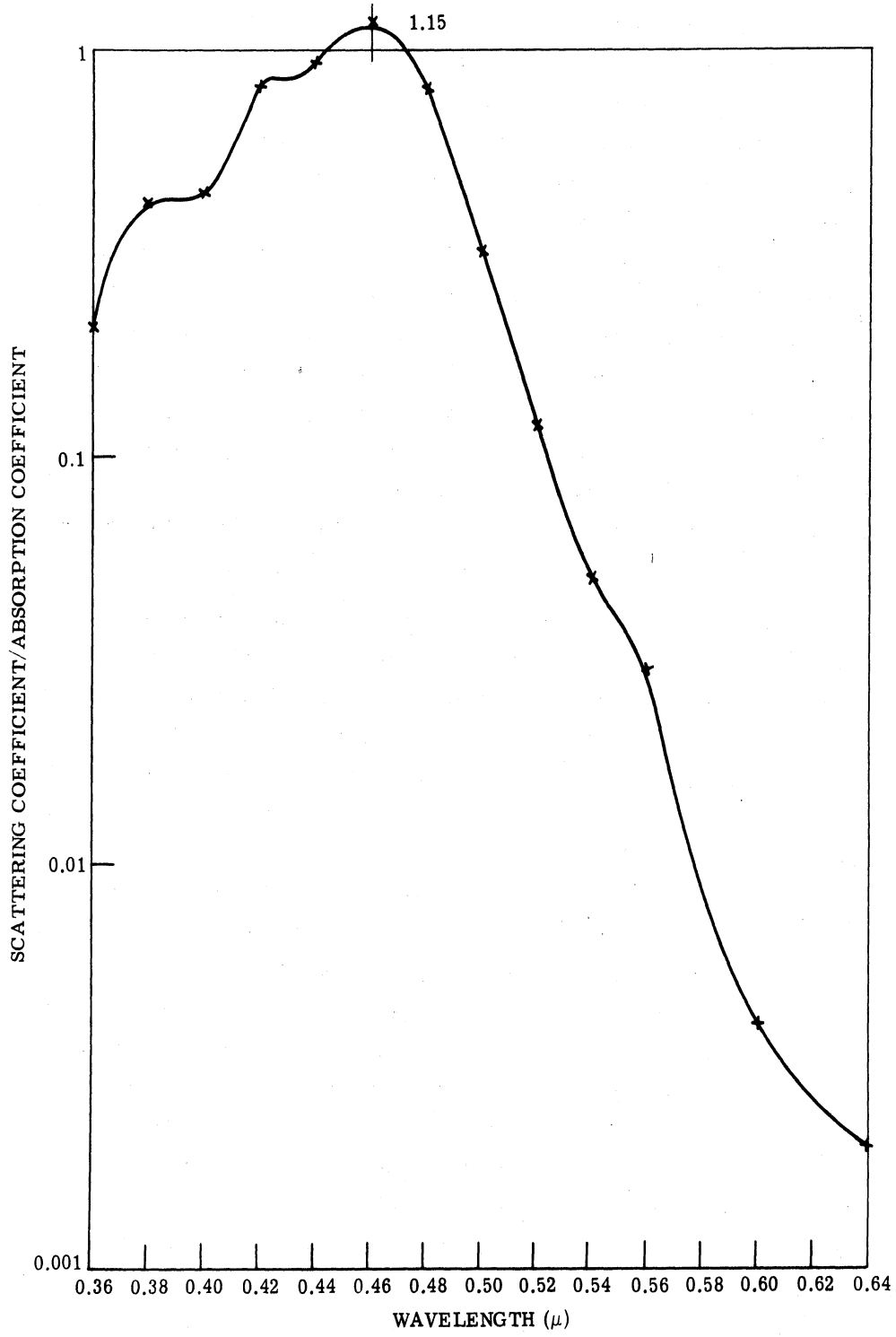

FIGURE 6. RATIO OF SCATTERING COEFFICIENT TO ABSORPTION COEFFICIENT VERSUS WAVELENGTH FOR PURE WATER

TABLE II. WAVELENGTHS OF MAXIMUM TRANSMITTANCE FOR PURE AND OCEAN WATERS [9, 10]

	Wavelength of Maximum Transmittance (μ)	Transmittance (%)	Total Attenuation Coefficient (α) (m^{-1})
Pure water	0.470	98.5	0.015
Clearest ocean water	0.470	98.1	0.0192
Average ocean water	0.475	89.0	0.1053
Clearest coastal water	0.500	88.6	0.1210
Average coastal water	0.550	72.4	0.3230
Average inshore ocean water	0.600	68.8	0.3857

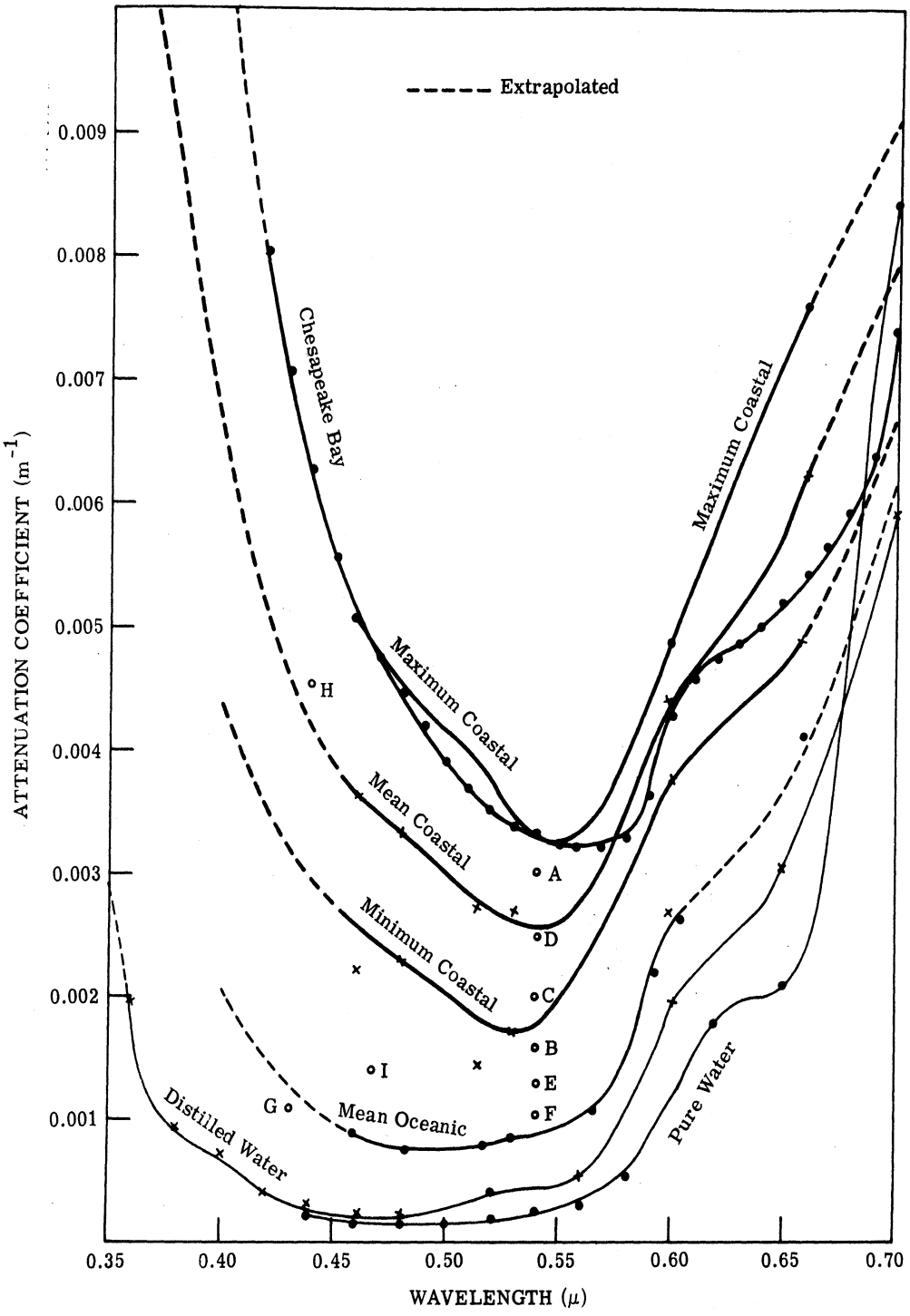

FIGURE 7. ATTENUATION COEFFICIENT VERSUS WAVELENGTH FOR PURE WATER AND SEA WATER

TABLE III. MEASURED ATTENUATION COEFFICIENT OF COASTAL WATERS IN 0.40- TO 0.55-μ REGION [11, 12]

Location	Depth (m)	Bandpass (μ)	Peak Response (μ)	Attenuation Coefficient (α) (m^{-1})
A. Woods Hole Harbor Lat. 41°31'N, Long. 70°40'W	20	0.4995-0.6000	0.54	0.30
B. Off Grey Head 41°20'N, 70°57'W	30	0.4995-0.6000	0.54	0.16
C. Vineyard Sound 41°30'N, 70°36'W	24	0.4995-0.6000	0.54	0.20
D. Buzzards Bay 41°33'N, 70°42.4'W	16	0.4995-0.6000	0.54	0.25
E. Off George Bank 40°48'N, 68°40'W	60	0.4995-0.6000	0.54	0.13
F. Gulf of Maine 42°68'N, 69°64'W	165	0.49-0.62	0.54	0.105
G. Gulf of Maine 42°08'N, 61°04'W	165	0.346-0.526	0.436	0.112
H. Gulf of Panama			0.440	0.453
I. Coastal water between Madeira and Gibraltar			0.465	0.139

to the number of particles suspended in the water. Near shore, there is a greater number of particles from rivers, and more can be suspended per unit volume. Bays and inland waters generally have even larger attenuation coefficients than coastal waters, as shown in table III. The clearest waters are found in mid-ocean regions where the amount of converging surface current and sinking is low. Ocean regions with diverging surface currents, which are accompanied by an upwelling of fertile deep water (high nutrient content), are more or less turbid as a result of high organic productivity. Clarke [16] found the attenuation coefficient of the Sargasso Sea to be as low as 0.017 m^{-1}. Coastal region waters, including waters surrounding the larger islands and the high-latitude waters, have the larger attenuation coefficients and in general are more turbid.

Except in the high latitudes, daylight supports the growth of phytoplankton mixed layers near the surface. These in turn feed a zooplankton population. The planktonic organisms range in size from microns to centimeters and scatter light which increases the scattering coefficient and thus the total attenuation coefficient of the sea water. Above the thermocline layer, the scattering coefficient varies with depth, the largest being nearest the surface. Likewise, any suspended particles (both organic and inorganic) in turbid coastal waters increase the scattering coefficient and the total attenuation coefficient. These particles originate from rivers, and their size and concentration vary with the seasonal rainfall and water currents. As shown in figure 7 for pure water, a uniform increase in the scattering coefficient (with the absorption coefficient remaining the same) will increase the height of the curve, but the greatest effect will be in the 0.42- to 0.58-μ region. The shift of the total attenuation minimum to longer wavelength and the increased value of the total attenuation coefficient are due to the increased scattering coefficient, while the absorption coefficient is almost totally independent of wavelength (non-Rayleigh scattering) because the distribution of suspended particles greatly favors particle diameters larger than visible wavelengths.

The effect of particle scattering on attenuation coefficient has been studied off the coast of Oregon at the mouth of the Columbia River [17]. In these measurements, the total attenuation coefficient (for white light) varied logarithmically from 2 m^{-1} at 1 mi to 0.1 m^{-1} at 100 mi off the coast because of the high turbidity of the water. (The water contained suspended clay silts and fine-grained sands carried by the Columbia River.) At Brooking, Oregon (280 mi south of the mouth of the Columbia River), the attenuation coefficient varied logarithmically from 0.17 m^{-1} at 1 mi to 0.1 m^{-1} at 100 mi off the coast. The effect of chlorophyll "a" particles on the attenuation coefficient for white light has also been measured [17]. The results generally conform to the theory of Riley which satisfies the following equation [18]:

$$\alpha = \alpha_{sw} + 0.0088\ C + 0.0546\ C^{2/3}$$

where α = total attenuation coefficient of sea water with chlorophyll (m^{-1})

α_{sw} = total attenuation coefficient of sea water without chlorophyll (m^{-1})

C = concentration of chlorophyll (mg/m^3)

The concentration of chlorophyll found off the coast of Oregon at three locations varied between 0.5 and 0.3 mg/m^3. Yentsch [19] and Tyler [20] show that the concentration of chlorophyll in pure water increases the value and shifts the minimum value of the attenuation coefficient, as shown in table IV [19].

TABLE IV. MINIMUM ATTENUATION COEFFICIENT AND ITS WAVELENGTH WITH CHLOROPHYLL "a" CONCENTRATION IN PURE WATER [19]

Concentration of Chlorophyll "a" (mg/m^3)	Minimum Attenuation Coefficient (α) (m^{-1})	Wavelength of Minimum α (μ)
0.5	0.021	0.4725
1.0	0.027	0.5080
3.0	0.037	0.5300
5.0	0.045	0.5400
10	0.062	0.5450
30	0.110	0.5490
50	0.160	0.5520
100	0.330	0.5530
200	0.520	0.5550

The monochromatic radiation wavelength for maximum-depth measurements in coastal and inland ocean water should be in the 0.5100- to 0.5800-μ region, as shown in figure 7 and in table III. Measurements using laser radiation at 0.5300 μ (the second harmonic of neodymium) indicate that any underwater measurements must use receiver fields of view of less than 2^o to exclude the multipath problem [12, 21]. Although the measurements in figure 7 are not monochromatic, the transmitter wavelength of a laser ranger can be selected.

3
WATER COLOR, DEPTH, AND ALGAL DISTRIBUTION

3.1. INTRODUCTION

As part of the inventory on the characteristics of shallow water and submarine features, documentation of water color, transparency, temperature structure, bottom type and color

spectrum (if possible), wave and swell climatology, etc., was requested from the National Oceanographic Data Center (NODC) as a function of station depth (where observed), time of year (month), and Marsden square. It was found that, while most of the parameters of interest were on the master cards for each Nansen cost on file, there was neither an atlas nor a complete inventory of the parameters and station locations which are on file at NODC. A parameter inventory was in preparation, but this would not be available before spring or summer 1968. Lepley [22], using unpublished Naval Oceanographic Office data, has shown that the distribution of water color and relative water clarity can be obtained from Gemini photography.

In the present program, water color has been treated as part of the total ecological environment involved with shallow-water features. Therefore, the influence of bottom type and alga type on the reflection of light that the sensor would see has been an important element in the detection problem. One question asked was, Can marine algae be used as depth indicators? It is known that algae grow in all the oceans of the world but are restricted to more or less "shallow" water (200 m). (Our definition of depth of interest as related to the navigational hazards of shallow water was Type A—soundings less than 100 ft, or approximately 30 m—as given in reference 1.) Many algae are visible much of the time because of tidal movements, and these algae show marked zonation patterns [23]. If algae which are always submerged are similarly zoned, could these zones be indicative of depth? There are multispectral sensors, such as those being developed at Willow Run Laboratories, which could be used to recognize species by their spectral signatures; thus, if there were an ecological relation to depth, then the depth might be inferred from the recognition. Even if there were not a reliable relationship of type with depth, it still would be useful to know the predominant species in likely areas and then to use the change in the observed color of the algae (due to the spectral losses in the light with depth) as a measure of the depth differences. As discussed in section 4, whenever a uniform bottom type is encountered over a varying depth, and uniform water transmission can be assumed, then a measure of depth change can be obtained from the change in density of a photograph or the change in electrical signal from a multispectral scanner.

The use of color as a shallow water indicator will most likely be based on several observations to establish persistence of a color feature and confirm the existence of shoal water indicated, perhaps, by wave refraction or temperature anomalies. Sometimes there can be significant persistence of open-ocean discolorations associated with upwellings and thermal fronts. Color structure associated with fronts appears as long streaks that could be interpreted as "extended reefs." It is by the convergence of evidence from different sensors that most of the misleading features will probably be eliminated.

One of the problems in studying depth indicators was defining the zero reference level and associated terms. The terms used in this investigation are given in the sketch in figure 8. The

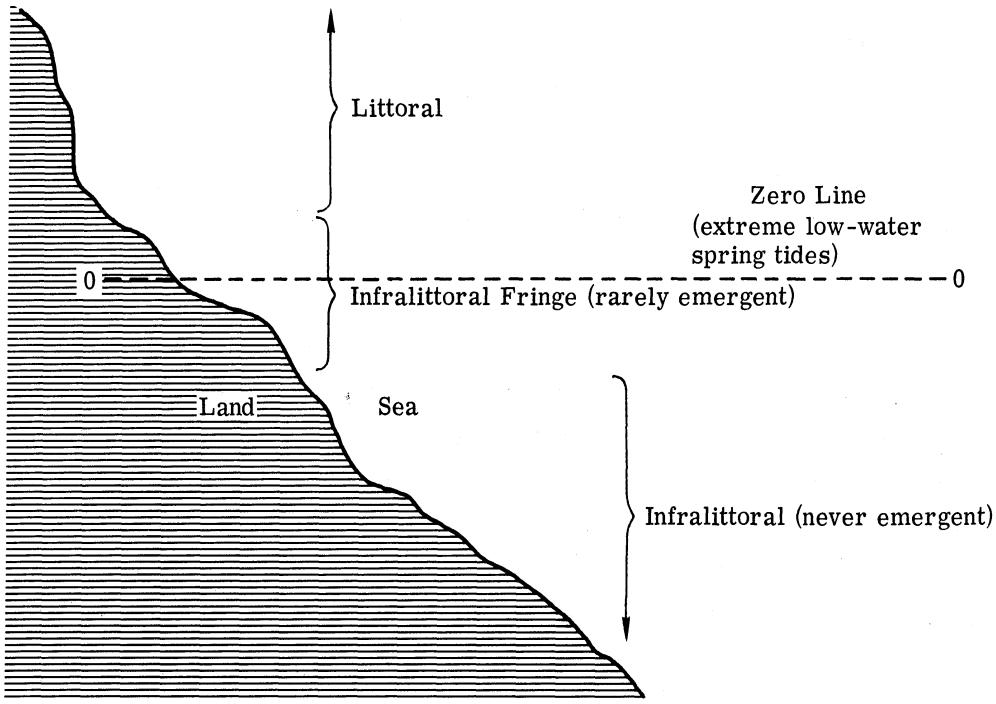

FIGURE 8. SKETCH FOR ZERO REFERENCE LEVEL AND ASSOCIATED TERMINOLOGY

littoral is the area between the high and low marks of most tides. (This zone, which is often subdivided, is not of concern here.) The infralittoral fringe is the area exposed only at the lowest spring tides. The infralittoral is the area that is always submerged. This terminology is related to other systems in use as follows:

Littoral	Intertidal	Littoral
Infralittoral fringe		Submerged littoral
Infralittoral	Subtidal	Sublittoral

3.2. ECOLOGICAL FACTORS

Many ecological factors influence algal distribution. The following are examples of the more important factors affecting distribution in the infralittoral fringe and in the infralittoral.

3.2.1. EMERGENCE. The infralittoral fringe is usually covered by some water, but it is exposed several times each year. It therefore supports

(1) Algae which require emergence during a small part of each year

(2) Algae which are facultative as to emergence

(3) Annual algae which require complete submergence, with their cycles beginning after the spring tides

The infralittoral bears

(1) Algae facultative as to emergence

(2) Organisms requiring continuous submergence

If the variation in species for the two zones is visible, there is likely to be a line of demarcation.

3.2.2. LIGHT. Light is necessary for all chlorophyllic plants, including marine algae. Each organism performs optimally at some given wavelength and quantity of light. As discussed in section 2, sea water absorbs various wavelengths of light to different degrees. The transmission maximum in most temperate coastal waters is in the green region, because of a dissolved "yellow substance" [24]. Marine algae contain one or more pigments which absorb light to be used in photosynthesis (fig. 9). All algae have chlorophyll, a green pigment with absorption maxima in the red and blue. Red algae contain phycoerythrin and phycocyanin;

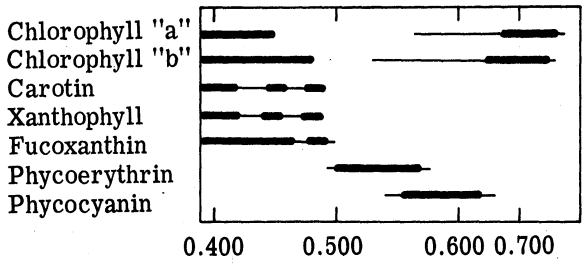

FIGURE 9. ABSORPTION OF VARIOUS ALGAL PIGMENTS [24]

the former pigment is red and absorbs green light, and the latter is blue and absorbs orange light. Brown algae contain fucoxanthin, a brown pigment which absorbs blue and some green wavelengths. Blue-green algae (not of concern here) contain predominantly phycocyanin. In general, then, green algae should require relatively shallow water because of the low transmission of red wavelengths by water. Brown algae, which are able to photosynthesize using green light, would be expected to grow in temperate coastal waters. Red algae, with absorption maxima in the red, green, and blue regions, should be able to grow at all depths but would have the least competition in deep, blue water and should be most abundant there. As will be seen, generalized zonations of this sort do occur (though of course there are many exceptions). For example, red algae predominate in blue tropical waters, brown algae in temperate coastal waters, and green algae in very shallow waters. Green algae, however, have been found in

very deep water (possibly due to their absorption peak in the blue region). Red algae can compete fairly well at all levels in many localities and so are not restricted to deep, blue water.

The above theory hypothesizes that algae respond to the transmitted wavelengths of incoming solar radiation [24]. Another theory [25] holds that the vertical distributions of algae are the result primarily of the value, rather than the spectral composition, of the total irradiance. The quantity of light is undoubtedly important for marine algae; more light penetrates on a clear, sunny day than on a cloudy day, and areas that have many cloudless days have deeper algal floras than do cloudy areas. However, it is to a large degree the wavelengths, penetrating to given depths, that determine the kinds of algae at those depths. Other factors which change the quantity of light and the depth of penetration are turbulence (less light is transmitted by a rough surface than by a smooth one) and the amount and size of suspended particles. A large amount of suspended material may be related to turbulence or may be sediment dumped by streams from the land.

3.2.3. TEMPERATURE. Mean sea-water temperatures for the warmest and coldest months and the annual variation in sea water temperature are important factors in the distribution of algae [26]. Sea temperature is directly related to air temperature in still water; the water surface temperature closely approaches the air temperature. The temperature either increases or decreases with depth, depending on the season. Thus, in the summer, quiet Mediterranean surface waters warm up considerably, and the terminus of the thermocline is quite deep. This causes some species to "retreat" to deeper water in the summertime. On an open, surf-beaten coast in summer, the cold water from beneath is constantly brought to the surface, and the water is more or less isothermal with depth throughout the year. Thus a deep species normally found in quiet waters may become established in shallow, but disturbed, waters.

Druehl [27] has studied the distribution of two Laminaria species with respect to temperature and salinity. L. groenlandica (long stripe form) can tolerate heavy surf and grows in areas of constant temperature and salinity. L. saccharina cannot tolerate surf and is facultative with respect to seasonal salinity and temperature variations (fig. 10). A cold-water current in an otherwise warm region of the earth can also cause a warm coast to have cold, and more or less constant, sea temperatures. An excellent example of this is the California current in the eastern Pacific. The terrestrial and littoral vegetation changes from cool temperate in British Columbia to subtropical in Baja, California. The infralittoral is subjected to a cold current which is relatively uniform throughout this distance. As a result, the infralittoral vegetation varies little with latitude.

Figures 11 and 12 show the depth locations of the dominant algae types (by color and name) for both cool and warm waters and different geographical areas. For cool temperate waters

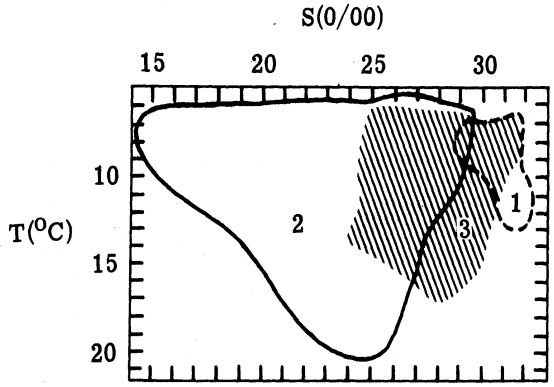

FIGURE 10. TOTAL RANGE OF SEASONAL SALINITY AND TEMPERATURE VARIATION FOR REGIONS OCCUPIED BY L. groenlandica (1), L. saccharina (2), AND L. groenlandica AND L. saccharina (3) [27]

(fig. 11), in the North Atlantic, brown algae are predominant at all depths and form extensive kelp beds. On unstable substrates, the green flowering plant Zostera forms extensive local beds. Pink calcareous algae occur less frequently and may form large beds that extend to greater depth than any of the other algae. In the cool temperate waters of the Pacific Ocean, the brown kelp Macrocystis is dominant and forms extensive beds (up to 100 mi long) in water 10 to 25 m deep. The "leaves" of this alga float on the surface and are visible from the air. The stems are attached to the sea bottom, so Macrocystis, unlike Sargassum,* should be a good depth indicator. Green algae are visible in a narrow band in very shallow water and alternate with beds of red Gigartina. The green flowering plant Phyllospadix forms carpets on rocky and sandy bottoms and in some areas excludes the browns from their usual habitats. In most cool waters, the maximum depth for abundant algal growth is about 25 m. Scattered individual algae go below this, and pink algae occasionally form carpets in much deeper water.

For warm waters (fig. 12), in the Gulf of Mexico area, only the infralittoral fringe and infralittoral reef flats have been adequately studied. In these areas, Thalassia, a green flowering plant, forms extensive carpets on sandy bottoms. On solid substrates, Laurencis (a red alga) forms a "yellowish green" carpet in shallow water [28]. Grey-green Halimeda (a calcareous green alga) may form extensive flats and even reefs. The pinks, mostly Lithothamnion, form extensive mats that extend into very deep water (100 m). The corals are common and form beds and reefs in water less than 50 m deep.

*The brown alga Sargassum often forms surface mats in the North Atlantic that extend for hundreds of miles. These mats do not indicate shallow water; the alga often floats on the surface of very deep water.

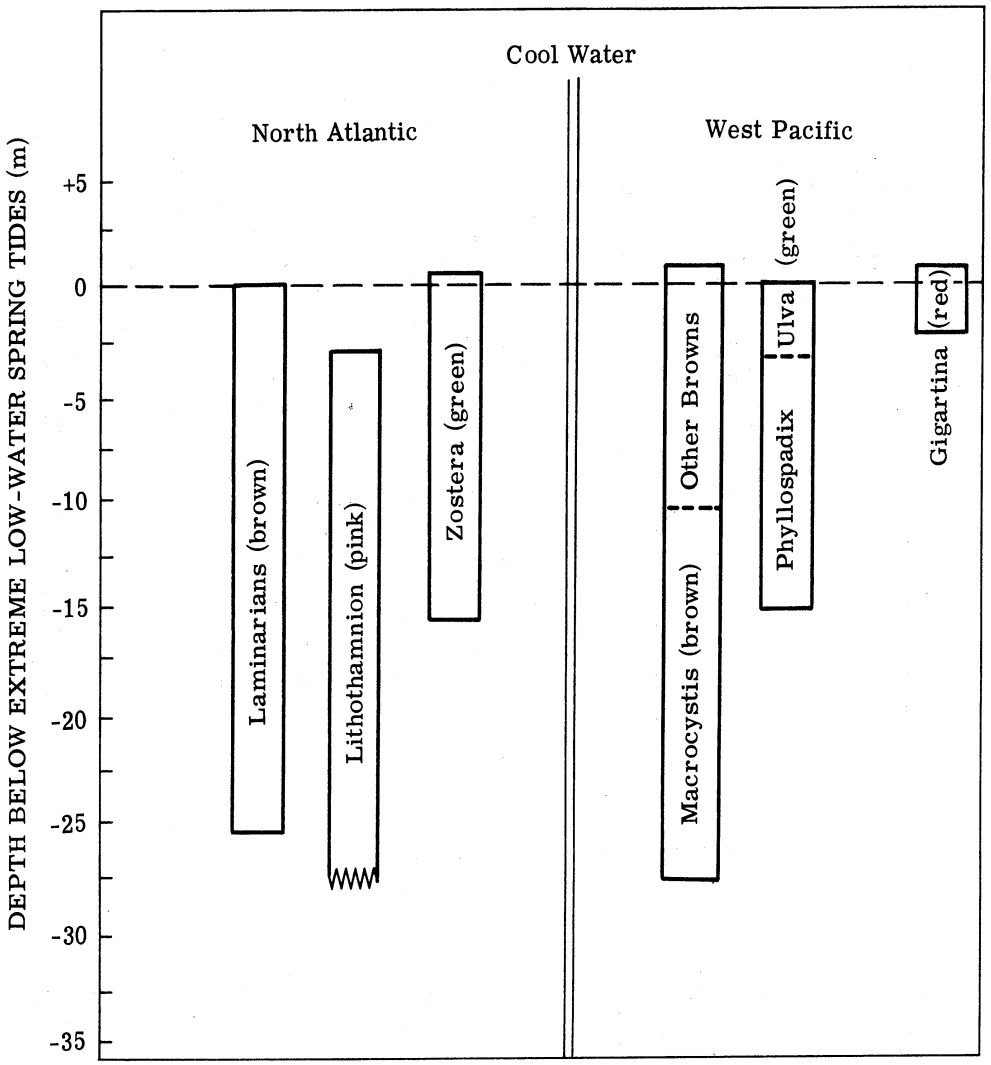

FIGURE 11. DEPTH DISTRIBUTION OF ALGAE IN THE NORTH ATLANTIC AND WEST PACIFIC

Green flowering plants predominate in the shallow waters throughout the Mediterranean; they grow on sand and mud, which are common in this region. The brown alga Cystoseira is predominant in the infralittoral fringe with solid substrate. Below this, the reds and mosaics of red-green-brown are predominant. In water deeper than 20 m, the pink Lithothamnion form extensive beds.

The Hawaiian algae (and those of the other Pacific islands) have not been adequately studied, from the point of view of this program. Green algae often cover barely submerged rocks. Pink calcareous algae predominate on the reef flats, and reds and a red-brown-grey-green-pink mosaic occur elsewhere.

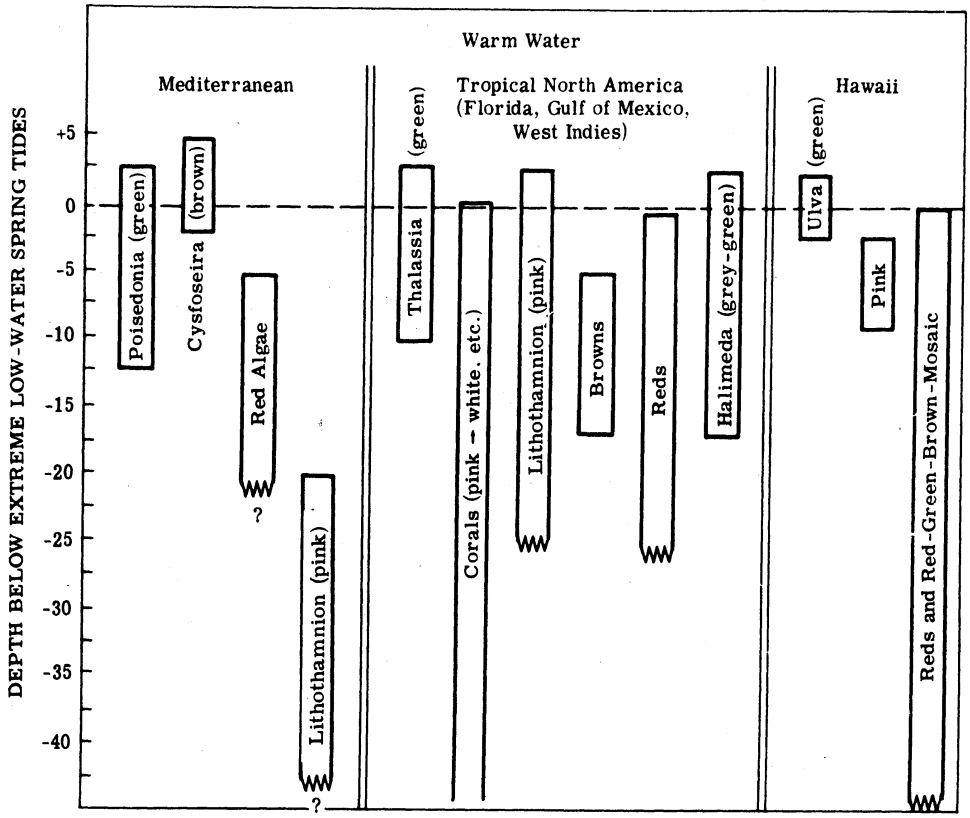

FIGURE 12. DEPTH DISTRIBUTION OF ALGAE AT VARIOUS GEOGRAPHICAL LOCATIONS

3.2.4. SEA ACTIVITY. Two major types of sea activity influence algal distribution: currents and surf. The effects of sea activity on light and temperature have been discussed above. There is, in addition, a physical effect. Some algae (e.g., L. saccharina) cannot tolerate surf conditions. Others require heavy surf to survive and propagate (a notable example being Postelsia palmaeformis, which grows only in surf-beaten areas off the California coast). Those which cannot grow in surf may either be too fragile to withstand the buffeting, or their immature stages may not be able to become attached. Those that must grow in the surf zone may not be able to compete in other areas.

3.2.5. SUBSTRATES. Algae do not have roots and use their substrates merely as places of attachment. Thus the chemical nature of the substrate has little or no effect on the alga. Yet the physical nature of the substrate is important in two ways: for its form (which includes stability and particle size) and for its shape (flat or inclined). Most algae will not grow on unstable substrates, such as sand or gravel. Those that do often cannot compete with other algae on the more stable substrates (rocks). Thus Laminaria saccharina predominates only in sandy

areas, while L. hyperborea grows only on solid rock. Both species inhabit the same regions. In the tropics, sandy areas are extensively carpeted with the flowering plant Thalassia. A similar situation occurs with Phyllospadix on the Pacific coast of the United States. The degree of slope of the substrate may be important in algal distribution. Kain [29] found that L. hyperborea may not grow in water shallower than 10 m on a substrate of boulders sloping more than 20^{0} to the horizontal; however, this is only an isolated case, and the problem needs further study.

3.2.6. SALINITY. Salinity may be constant over an area, or it may vary seasonally and with depth. Druehl [27] has shown that L. groenlandica tolerates less salinity variation than L. saccharina (fig. 10). In the fjords of Norway, salinity fluctuates because of seasonal runoffs of fresh water from the land; Jorde and Klavestad [30] have shown that the algal flora progressively diminishes as the salinity amplitude increases. The species composition changes strikingly with these fluctuations, especially in shallow water. For example, Pylaella occurs in areas characterized by extreme amplitudes but not elsewhere in the fjord.

3.2.7. PERIODICITY. Marine algae do, of course, show seasonal periodicity. Some algae are annuals, some are perennials. The annuals "bloom" just as land plants do. This effect is less noticeable in the infralittoral than in the littoral but does occur. In general, in the northern hemisphere, regrowth of a flora begins in February and climaxes in midsummer. The seasons are not well-defined in the tropics. Algae that grow all year in the Mediterranean may grow only in the summer in the cold northern waters. The opposite is true of psychrophyllic algae (i.e., they grow all year in northern waters and only in winter in the Mediterranean).

3.3. GENERAL GEOGRAPHY OF INFRALITTORAL ALGAE

Cool temperate shores have predominantly large, brown algae (see sec. 3.2.3). In the Atlantic, Laminaria is the principal component. In the Pacific, Laminaria inhabits shallow water, and Macrocystis and Nereocystis grow in deeper waters. Antarctic shores have very deep floras of Durvillea and Desmarestia, with only encrusting red algae in the infralittoral fringe. Little is known of the Arctic algal flora. Warm temperate regions are usually characterized by Cystoseira, many red algae, and extensive beds of flowering plants (Poisedonia in the Mediterranean, Phyllospadix on the Pacific coast, and Thalassia in Florida). South Africa has a turf of red algae and occasional areas of Sargassum. In the Australian infralittoral, the predominant algae are Ecklonia and Phyllospora in New South Wales, Sarcophycus in Victoria, Cystophora along the southwestern coast, and Sarcophycus and Lessonia in Tasmania. New Zealand infralittoral zones bear Ecklonia, Sargassum, and Lessonia, with Durvillea predominant on the western coast. Near Portobello, New Zealand, the predominant alga in the infra-

littoral is Macrocystis. Tropical zonation is often disturbed by reef formation (see sec. 3.3.1.6). A normal infralittoral pattern is found in West Africa (Ecklonia, Gracilaria, Dictyota, Cystoseira), St. Helena (Laurencia and Corallina), the West Indies (Thalassia and Halimeda, and a profusion of other species), South America (Sargassum and Padina), and Malaya (Halimeda, Padina, Caulerps, and Sargassum).

3.3.1. SPECIFIC AREAS

3.3.1.1. The British Isles. Predominant in the infralittoral fringe are Laminaria digitata, Himanthalia lorea, and, on wave-beaten shores, Alaria esculenta. These are replaced 1 m below low-water spring-tide levels by L. hyperborea on solid rock (disturbed water) and L. saccharina on sand or stones (quiet water). These species extend to a depth of 6 to 20 m, depending on the locality. Water turbidity and the absence of deep rock are the main factors influencing maximum depth. Kain [29] has studied the infralittoral flora of the Isle of Man; her data are summarized in figure 13. The L. hyperborea forest obscures all other algae growing in it; thus, if any of the other three algae were sighted, the most probable ocean depth would be below the forest (greater than 13 m). Table V summarizes the depth data from Forster [31], Kain [32], Kitching [33], and Walker [34]. In all cases, Laminaria species predominate in almost the entire infralittoral.

3.3.1.2. The Northwest Atlantic. Laminaria, Alaria, and Agarum predominate along the Nova Scotia shore. Table VI compares the depths of these algae [35]. Colvinaux [36] presents a list of algae from Massachusetts, New Brunswick, and Labrador comparing their depths at the three localities. This list is included in its entirety in table VII. It shows clearly that the depth at which an alga grows can change with latitude.

3.3.1.3. Norway (Hardangerfjord). The exposed Norwegian coast has algal vegetation similar to that of the British Isles. In the infralittoral fringe, Alaria predominates on surf-beaten shores and Himanthalia is predominant elsewhere. In the infralittoral, there is a zone of L. digitata and below this L. hyperborea and L. saccharina. Lithothamnion encrusts deeper rocks. Table VIII summarizes the depth data for this area [30]. Within the fjords, the vegetation changes drastically. The water is quiet and is subject to large temperature and salinity amplitudes. The infralittoral fringe is covered with Fucus serratus. The infralittoral is covered with L. saccharina, Desmamestia aculeata, and in areas of extreme salinity amplitudes, Pylaella. The lower vegetation limit is generally about 30 m outside the fjord and 10 to 15 m within. The shallower limit presumably is caused by lack of water movement [30].

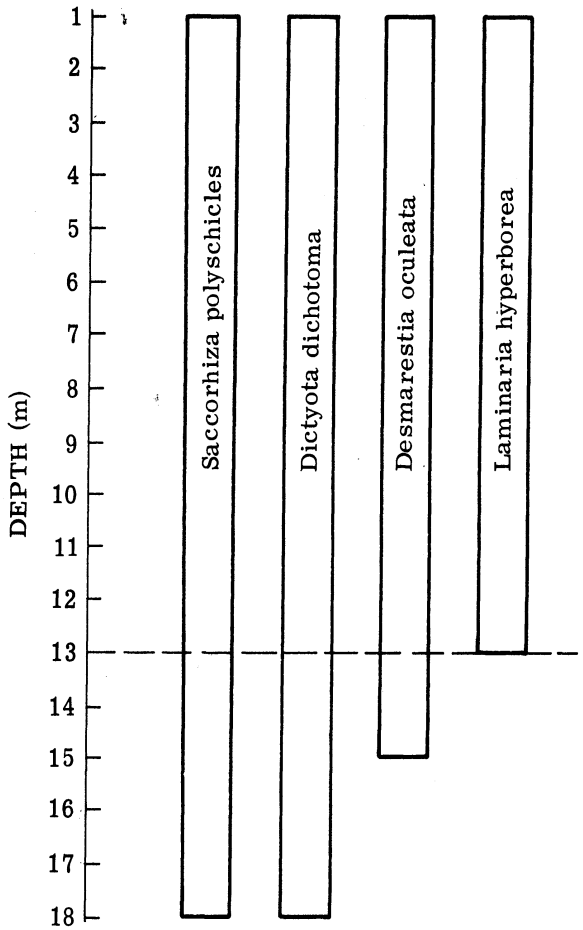

FIGURE 13. DEPTH DISTRIBUTION OF L. hyperborea AND THREE ASSOCIATED ALGAE, ISLE OF MAN [29]

3.3.1.4. The Pacific Coast of North America. The infralittoral region of the Pacific coast is remarkably uniform from Puget Sound to Baja, California. While the littoral is affected by the gradual climatic change from cool north temperate to subtropical, the infralittoral is controlled by the cold water predominating offshore on this entire shore line. The major infralittoral algae are Laminaria, Macrocystis, and Nereocystis. The infralittoral fringe changes considerably from northern California to Monterey. The infralittoral fringe at Monterey and Carmel is characterized by a solid crust of Calliarthron overgrown with Dictyoneurum, Cystoseira, Desmarestia, and Egregia. Sandy areas at San Francisco, Monterey, and La Jolla (0 to 7 m) are dominated by Phyllospadix. It is likely that the infralittoral fringe undergoes further change southward, but there have been no ecological studies to substantiate this. Most depth data collected for this coast are for the large, economically important kelp

TABLE V. SUMMARY OF DEPTH DATA FOR THE ALGAL FLORA OF THE BRITISH ISLES [31-34]

	Maximum	Minimum	Localities
Laminaria hyperborea	13 m	1 m	Isle of Man
	17	1	Stoke Point
	6	1	Dartmouth
Laminaria cloustoni	16	2	Orkney Isles
	15	0	Carsaig Island
Desmarestia aculeata	15	1	Isle of Man
	15	6	Carsaig Island
Dictyota dichotoma	18	2	Isle of Man
	8	6	Dartmouth
Sacchoriza polyschides	18	1	Isle of Man
Dictyopteris membranacea	25	17	Stoke Point

TABLE VI. SUMMARY OF DEPTH DATA FOR THE ALGAL FLORA OF NOVA SCOTIA [35]

	Maximum	Minimum
Laminaria longicruris	9 m	0.5 m
Laminaria digitata	10	0
Alaria exculenta	1	0
Agarum cribrosum	18	7

TABLE VII. VERTICAL RANGES OF A NUMBER OF ALGAE IN MASSACHUSETTS, THE BAY OF FUNDY, AND LABRADOR-NORTHWEST NEWFOUNDLAND ILLUSTRATING CHANGE OF DEPTH WITH CERTAIN LATITUDES [36]

Species	Massachusetts	Bay of Fundy, N.B.	Labrador-Newfoundland
Chaetomorpha linum	6-12 m below MLTL*	Upper half of lit.	—
C. melagonium	3-5 m below MLTL	Lower lit, incl. pools, sublit.	Low lit. incl. pools sublit.
Agarum cribrosum	10-20 m below MLTL	Upper sublit. & down	Low lit. pools, sublit.
Desmarestia aculeata	6-8 m below MLTL	Upper sublit. & down	Upper sublit. down.
D. viridis	6-8 m below MLTL	Upper sublit. & down	—
Laminarias	2-12 m below MLTL	Lower lit. pools, upper sublit. & down	Low lit. pools, sublit.
Petalonia fascia	Sublit. fringe & upper sublit.	Mid-lower lit. incl. pools	Mid-low lit. pools, at and below low-tide
Saccorhiza dermatodea	About 2 m below MLTL (rare)	Low lit. pools, upper sublit. & down	Sublit.
Scytosiphon lomentaria	Sublit. fringe & upper sublit.	Mid and low lit.	Mid-low lit. pools, at & below low-tide
Ceramium rubrum	~2-12 m below MLTL	Pools lower half of lit., upper sublit.	—
Corallina officinalis	~2-12 m below MLTL	Lower half of lit., upper sub-lit. & down	—
Cystoclonium purpureum	~2-13 m below MLTL	Pools lower lit.	—
Euthora cristata	~4-14 m below MLTL	Upper sublit. & down	Low lit. pools, upper sublit. & down
Halosaccion ramentaceum	~2 m below MLTL	Pools lower lit.	Lower lit. incl. pools, at & below spring tide
Membranoptera alata	~13 m below MLTL	Upper sublit. & down	Low lit. pools, sublit.
Phycodrys rubens	~7-11 m below MLTL	Tide pools lower lit., upper sublit. & down	Low lit., pools, upper sublit. & down
Phyllophora brodiaei	6-20 m below MLTL	Pools lower lit., upper sublit. & down	Sublit.

*MLTL: mean low tide level

TABLE VIII. SUMMARY OF DEPTH DATA FOR THE ALGAL FLORA OF THE COAST OF NORWAY [30]

	Maximum	Minimum
Alaria	1 m	0 m
Himanthalia	1	0
Laminaria digitata	5	1
Laminaria hyperborea	7	5
Laminaria saccharina	7	5
Lithothamnion		7

beds offshore; thus, from 7 to 25 m, the floras are quite well documented. Table IX summarizes the depth data of Aleem [37], Andrews [38], McClean [39], and Neuschul [40]. At a depth of about 7 m, the giant kelp beds begin and extend to about 30 m. The beds would probably obscure any undergrowth when viewed from above. The kelp grows to 100 ft in length and the "leaves," even in deep water, trail on the surface and are readily visible from the air. Macrocystis species predominate in shallow water and quiet, deep water, while Nereocystis is predominant in deeper water subject to tidal currents.

3.3.1.5. Florida. The Stevensons [28] have studied coral reefs in the Florida keys. Their work deals mostly with intertidal areas, and they do not cite specific depths. They do discuss a "reef flat" which is permanently submerged but shallow (mostly less than 1 m but up to 7 m deep). The flowering plant Thalassia forms extensive carpets in this area. Many areas have no algae. Those areas with algae have a mixture of the following:

Caulerpa
Dictyota
Cladophora
Halimeda
Penicillus
Dictyota
Sargassum
Laurencia
Lithothamnion

3.3.1.6. Hawaii. The distribution of Hawaiian marine algae is intimately associated with coastal topography and the development of coral reefs and shallows [41]. Where there is no

TABLE IX. SUMMARY OF DEPTH DATA FOR THE ALGAL FLORA OF THE WEST COAST OF THE UNITED STATES [37-40]

	Maximum	Minimum	Localities
Phyllospadix scouleri	7 m	0 m	LaJolla (sand)
Macrocystis pyrifera	25	7	Monterey Bay (sand)
Macrocystis integrifolia	12	6	Monterey
Pelagophycus porra	30	20	LaJolla
Pterygophora	20	7	LaJolla
	15	6	Monterey
	15	7	Puget Sound
Laminaria	20	7	LaJolla
	9	3	Monterey
Eisenia	20	7	LaJolla
Nereocystis leutkeana	15	10	Monterey
	18	4	Monterey
	3	0	Puget Sound
Calliarthron cheilosporioides	3	0	Monterey
Dictyoneurum californicum	3	0	Monterey
Cystoseira	3	0	Monterey
Desmarestia	3	0	Monterey
	12	10	Puget Sound

reef, the land drops off sharply and the water is too deep for study. Table X is a brief summary of the depth data for the algal flora of a coral reef. Coralline algae such as Lithothamnion and Halimeda are very important in reef building under certain circumstances. These algae can flourish and build reefs at depths of 450 to 630 m, whereas corals are limited to a maximum of 45 to 72 m; they are also much less dependent than corals on high temperatures.

3.4. CONCLUSIONS

Algae grow at specific depths, depending on a number of ecological factors. Most depth ranges are relatively wide (up to 15 m), but a few algae in the infralittoral fringe are restricted to zones 1 m or less in width. In a few instances, alga types identified at the surface give an indication of depth; for example, the presence of the brown kelp Macrocystic implies depth of 10 to 25 m. Where a particular alga type grows at various depths, it becomes useful in terms of a known spectral reflectance percentage and thus aids in mapping features through multispectral techniques (sec. 4). The literature is inadequate in supplying necessary depth data

for most areas of the world. It will be necessary to conduct studies specifically for the purposes of clarifying ecological changes with depth and compiling a catalog of indicator species and their ecological requirements.

TABLE X. SUMMARY OF DEPTH DATA (WHERE KNOWN) FOR THE ALGAL FLORA OF A HAWAIIAN CORAL REEF

	Maximum	Minimum	Localities
Enteromorpha	1 m	0.5 m	Inshore waters
Gracilaria	1	0.5	Coral sand or mud
Sargassum			Coral rocks
Gracilaria			Coral rocks
Gelidium			Lava blocks
Ahnfeldtia			Lava blocks
Lithothamnion			
Corallina			
Peysonnelia	10	1	Lagoon pools
Grateloupia			
Ceramium, etc.			
Corallines	10	3	Lagoon
Haliseris			
Dictyota			
Codium			
Asparagopsis			
Gymnogongrus			
Porphyra	1		Outer reef rim
Turbinaria			
Gelidium, etc.			

4
MULTISPECTRAL SENSING

4.1. USE OF MULTISPECTRAL SENSING TO DETERMINE DEPTH

One of the more promising techniques that may be used to map color differences, determine algal types, and compute the depth of water involves the use of two or more channels of data that measure the spectral signature for each element observed under water. A sensor system that can implement this technique is under development by Willow Run Laboratories. This system

presently obtains data in 18 channels spaced between 0.3 and 15 μ. Data in the visible region are obtained simultaneously in 12 different regions between 0.4 and 1.0 μ. The spectrometer mounted in the scanner represents an advantage in spectral filtering over the use of color film in cameras because, with the former, a mechanical method is employed to select the wavelength interval, whereas with the latter, dyes and emulsions are used whose spectral responses are generally broad-band and not well defined. The multispectral scanner is also superior to multiple cameras with different film/filter combinations because, with the scanner, the time and space synchronization for each resolution element is assured, and this permits the use of automatic pattern-recognition schemes in the analysis of the large amounts of data expected to be obtained with satellites or aircraft. Cameras can provide better resolution but only if the film can be retrieved from the spacecraft and (if the phenomena under study require such resolution) resources are available for the sorting and interpretation efforts involved.

Illustrative of the type of data that can be obtained with a multispectral scanner are the images (showing bottom details) in figures 14-17. The area imaged is off the Florida Keys near Carysfort Reef and Pacific Reef. These figures show data from only a few of the channels in order to illustrate the effect of wavelength on the quality of the imaging. Note that the best detail is seen in the 0.55- to 0.58-μ regions, while only land above the water surface or white foam, etc., are shown in the 0.8- to 1.0-μ region. In the region 0.62 to 0.66 μ, only the shallowest points are observed, while in the blue region, 0.40 to 0.44 μ, scattering of light tends to lower the contrast of objects beneath the water. Much work is being done to try to relate density on film to depths of water. The amount of light reflected back to the sensor is the product of several factors, including the transparency of the water and the reflectance of the bottom material. Therefore one must be careful to distinguish a given density on film as the result of light coming either from a strong reflector at a relatively greater depth or from a weak reflector at a relatively shallow depth, both of which may give the same density. Only in the areas where bottom type and water clarity are uniform can there be a reliable correlation between density and depth of water.

Consider the relationship of energy collected by the sensor to the various parameters involved in the measurement. Let the power collected by the sensor be P and the electrical signal proportional to it be V. Then, in a single spectral channel,

$$V = K\rho H e^{-\alpha(\cos^{-1}\theta+\cos^{-1}\phi)z} \qquad (2)$$

where V = signal in channel of bandwidth $\Delta\lambda$

ρ = reflectance of bottom material in that wavelength interval

H = irradiance of the sun at the water surface

α = water extinction coefficient

z = depth of the water

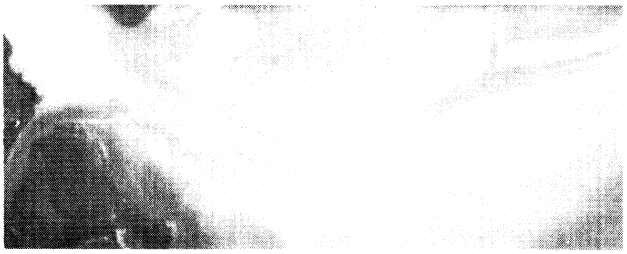

0.40-0.44 μ

0.55-0.58 μ

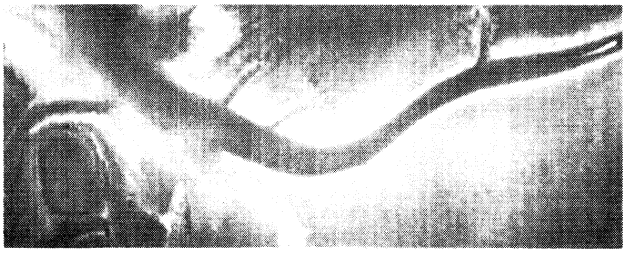

0.62-0.66 μ

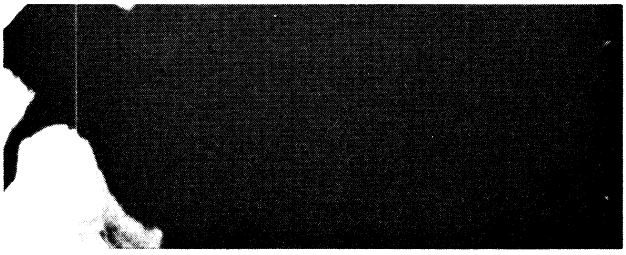

0.8-1.0 μ

FIGURE 14. FOUR-CHANNEL MULTISPECTRAL IMAGERY, CAESAR CREEK, ALTITUDE 2000 ft

0.40-0.44 μ

0.55-0.58 μ

0.62-0.66 μ

0.8-1.0 μ

FIGURE 15. FOUR-CHANNEL MULTISPECTRAL IMAGERY, PACIFIC REEF, ALTITUDE 2000 ft

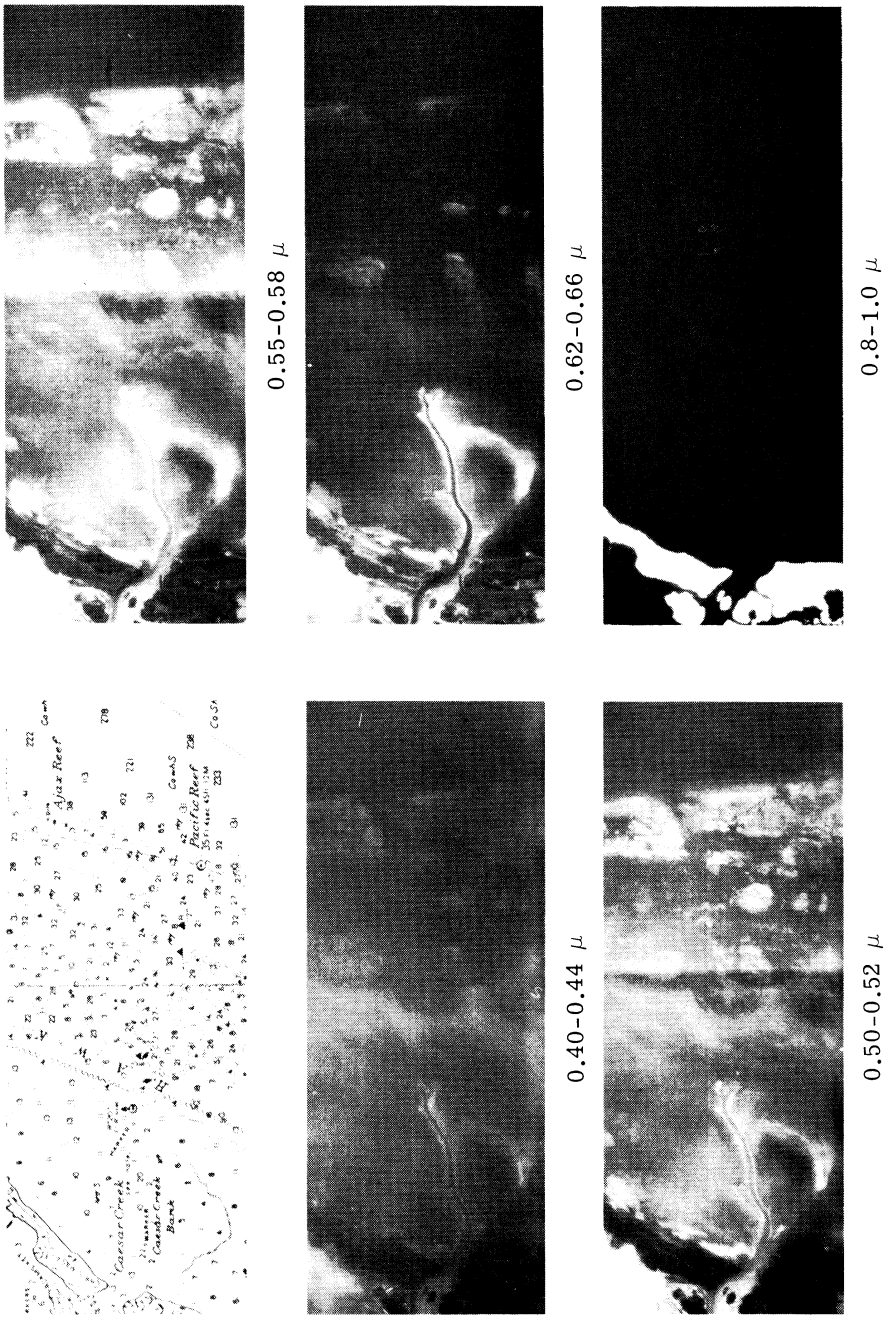

FIGURE 16. FIVE-CHANNEL MULTISPECTRAL IMAGERY, PACIFIC REEF, ALTITUDE 10,000 ft

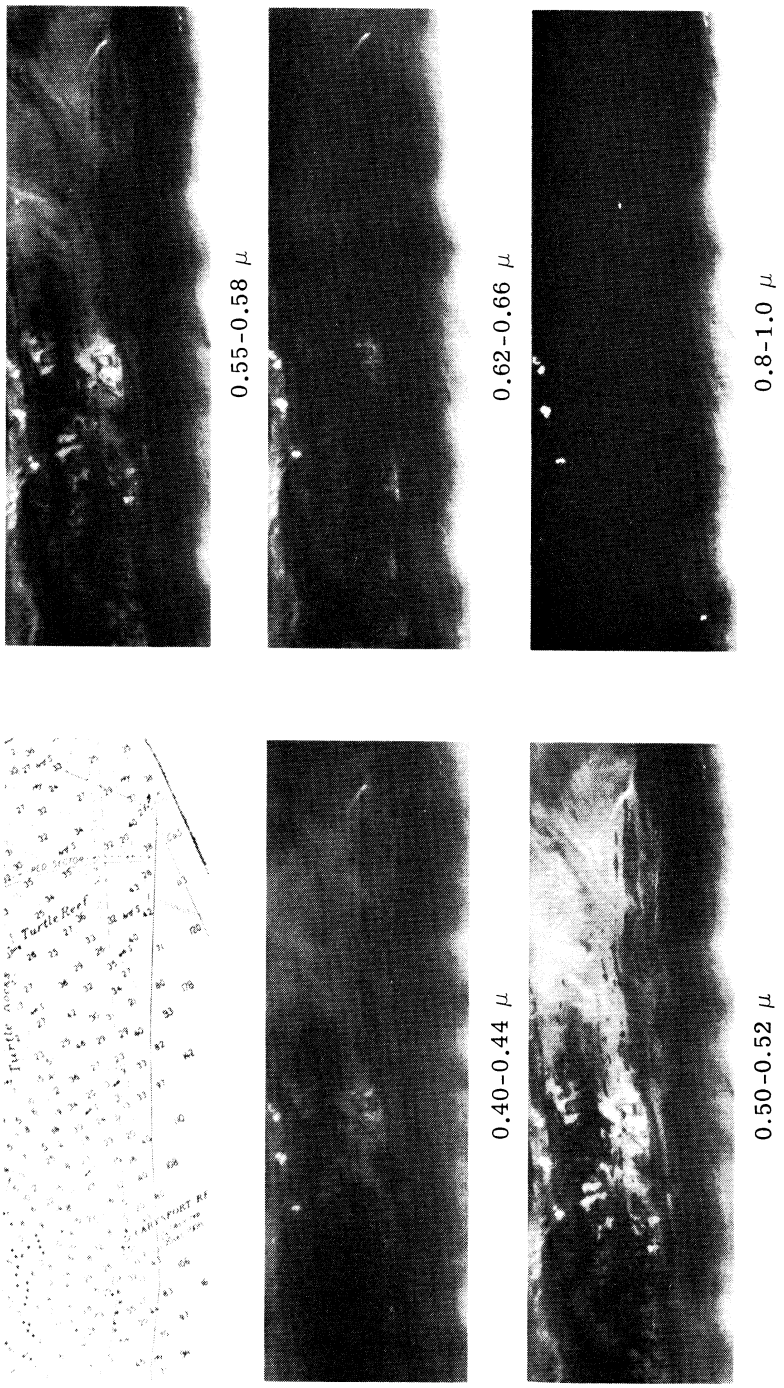

FIGURE 17. FIVE-CHANNEL MULTISPECTRAL IMAGERY, CARYSFORT REEF, ALTITUDE 10,000 ft

θ = known angle of incidence

ϕ = viewer observation angle

K = function of other known quantities, i.e., of receiver size and field of view, responsivities, transmission of atmosphere, and optics

For single-band operation, it can be readily observed that for two different but proximate locations on successive scans (with the same illumination, observation angle, water transmission, and bottom reflectance characteristics),

$$\frac{V_1}{V_2} = \frac{e^{-\alpha z_1(\cos^{-1}\theta + \cos^{-1}\phi)}}{e^{-\alpha z_2(\cos^{-1}\theta + \cos^{-1}\phi)}}$$

Then

$$z_2 - z_1 = \frac{1}{\alpha f(\theta, \phi)} \ln \frac{V_1}{V_2}$$

when $f(\theta, \phi) \equiv \cos^{-1}\theta + \cos^{-1}\phi$, which can be computed, since the angles of incidence and observation are known quantities. Since V_1 and V_2 are obtained from the sensor, a computation of depth difference is possible. The sensor (in conjunction with a laser depth-ranging system—see sec. 7—which would provide an absolute depth measurement at several points along a path) may be used to map the profiles of features in shallow waters to a depth which is dependent on many system design tradeoffs and consideration of size and cost.

The full potential of the multispectral method (besides the automatic recognition and the improved spectral filtering) lies in the possibility of computing absolute depth using two or more spectral channels. Consider equation 2 again, but now, instead of using one channel at two different points along a path, calculate the signal from two channels for the same resolution element and form a ratio:

$$\frac{V_{\lambda_1}}{V_{\lambda_2}} = \frac{K_{\lambda_1}\rho_{\lambda_1}H_{\lambda_1}e^{-\alpha_{\lambda_1} z(\cos^{-1}\theta + \cos^{-1}\phi)}}{K_{\lambda_2}\rho_{\lambda_2}H_{\lambda_2}e^{-\alpha_{\lambda_2} z(\cos^{-1}\theta + \cos^{-1}\phi)}}$$

where the quantities are defined as above, except that now their spectral dependence at two different wavelength intervals must be considered. Solving for z,

$$z = \frac{1}{f(\theta, \phi)\left(\alpha_{\lambda_2} - \alpha_{\lambda_1}\right)} \ln \frac{V_{\lambda_1} K_{\lambda_2}\rho_{\lambda_2}H_{\lambda_2}}{V_{\lambda_2} K_{\lambda_1}\rho_{\lambda_1}H_{\lambda_1}}$$

Given an expression for absolute depth, let us now see if a practical measurement is possible. We are at liberty to choose the wavelengths we desire. The solar irradiance H_{λ_1} and H_{λ_2} can be measured under different conditions and the ratio $H_{\lambda_2}/H_{\lambda_1}$ computed. Because of their different absorption characteristics, the red and blue wavelength regions can be used to make $\alpha_{\lambda_2} - \alpha_{\lambda_1}$ a relatively large quantity, for better accuracy. Now V_{λ_1} and V_{λ_2} are the quantities measured during sensor operation, and K_{λ_1}, K_{λ_2}, and $f(\theta, \phi)$ are computed based on known quantities of sensor size, responsivity, angles of incidence and observation, etc. What remains is to determine a ratio of the reflectance (ρ) of the bottom material for two different wavelengths. For some sands, this ratio, at the wavelengths chosen, may be unity, or, if we know the material type from ecological and geographical considerations, the ratio can be calculated. This hypothesis was tested in an approximation using the data of other researchers who obtained measurements of radiation reflected from sandy bottom at different depths. Estimated values of water transmissivity and reflectivity of sand were used, and the accuracy of the depth calculation was encouraging. (We have not performed an analysis of the multispectral scanner data because of time and cost limitations under the present contract.)

The results of preliminary processing of a small portion of the data taken off the Florida reefs are shown in figure 18. Two-channel processing using a light-pencil method [42] was performed; this processing amounts to color recognition of underwater features using two spectral intervals (figures 18a, b, and c); figure 18d presents the result of a one-channel analysis showing a "density" slice. Comparison with the depth soundings in figure 17 shows that water depth of 13 ft or less is recognized.

4.2. OPTICAL-MECHANICAL SYSTEM TRADEOFF STUDY

A parametric analysis of an optical-mechanical scanner was conducted to determine the requirements for obtaining data for water depth determination and for mapping details of underwater features. Figures 19 and 20 summarize the results for an aircraft at 1000 ft and for a 200-nmi satellite and aircraft at 10,000 ft. The analysis permits estimation of the size of the primary collecting aperture (a measure of the cost and complexity of the sensor), for a given water-transmissivity value, that would be required to recognize a small change in the light reflected from the bottom at a given depth and with a reasonable signal-to-noise ratio (SNR). For example, from a 200-nmi orbit, an optical-mechanical sensor with a 1-mrad instantaneous field of view would require a 5-cm diameter collector in order to see a change in bottom reflection of 10 percentage points (for SNR = 3 at 0.55 μ) at a depth of 7.5 m in coastal waters or at a theoretical maximum of 30 m considering distilled-water clarity. However, the ground resolution would be approximately 1200 ft (400 m), and in order to map smaller shoal areas, a

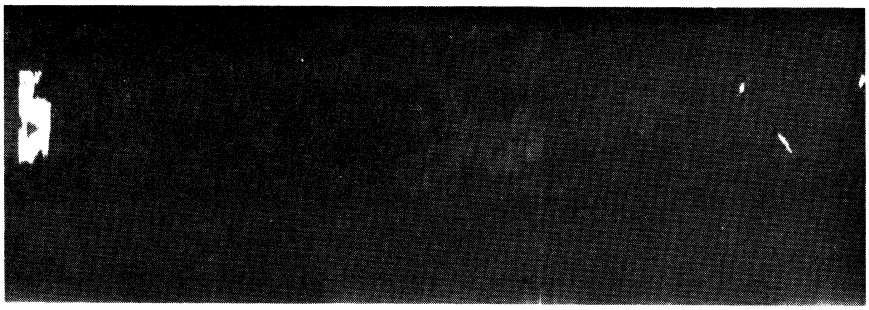

(a)

(b)

(c)

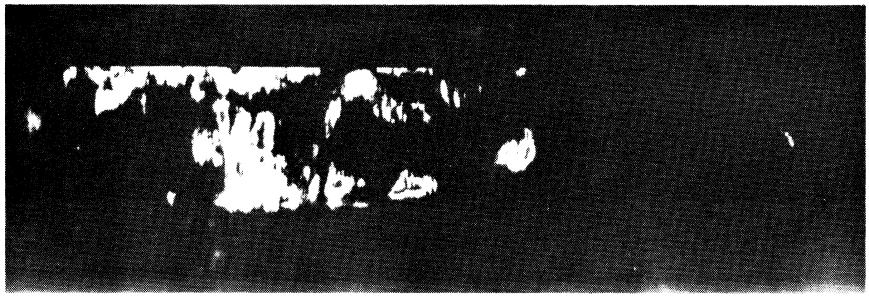

(d)

FIGURE 18. PRELIMINARY RESULTS OF ONE- AND TWO-CHANNEL PROCESSING. Three different underwater features are mapped in parts a, b, and c.

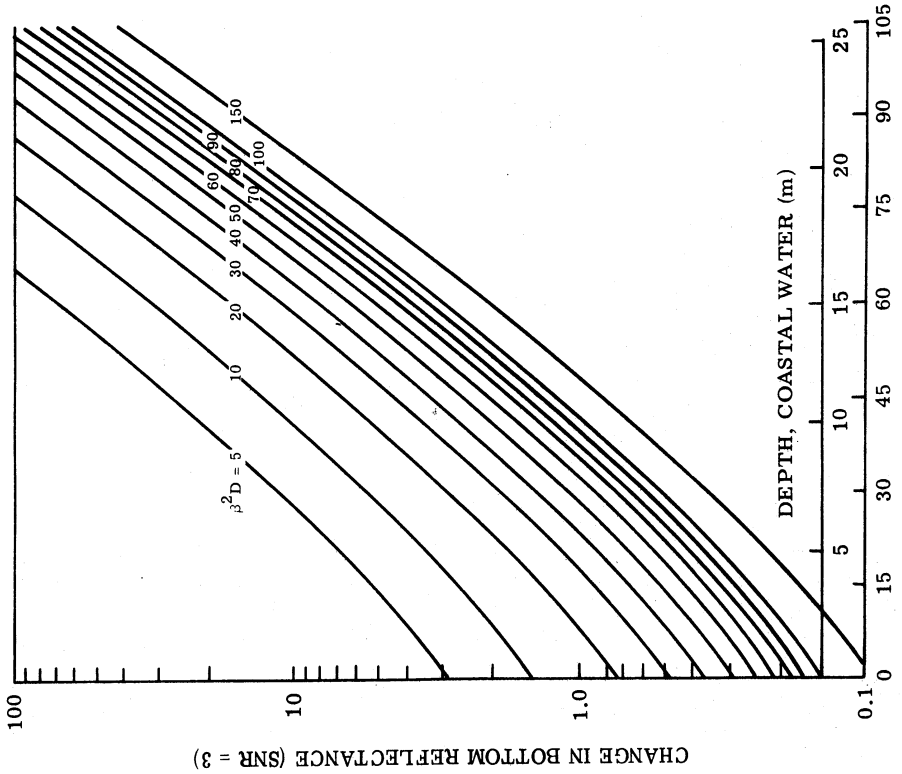

FIGURE 20. PARAMETRIC CURVES RELATING DESIGN, CHANGE IN BOTTOM REFLECTANCE, AND WATER DEPTH FOR THE AIRCRAFT SYSTEM AT 10,000 ft AND THE 200-nmi SATELLITE SYSTEM Bright sunlight; $v/h = 0.02\ sec^{-1}$, $\Delta\lambda = 545\text{-}555\ m\mu$; β in mrad, D in cm; S-20 photocathode.

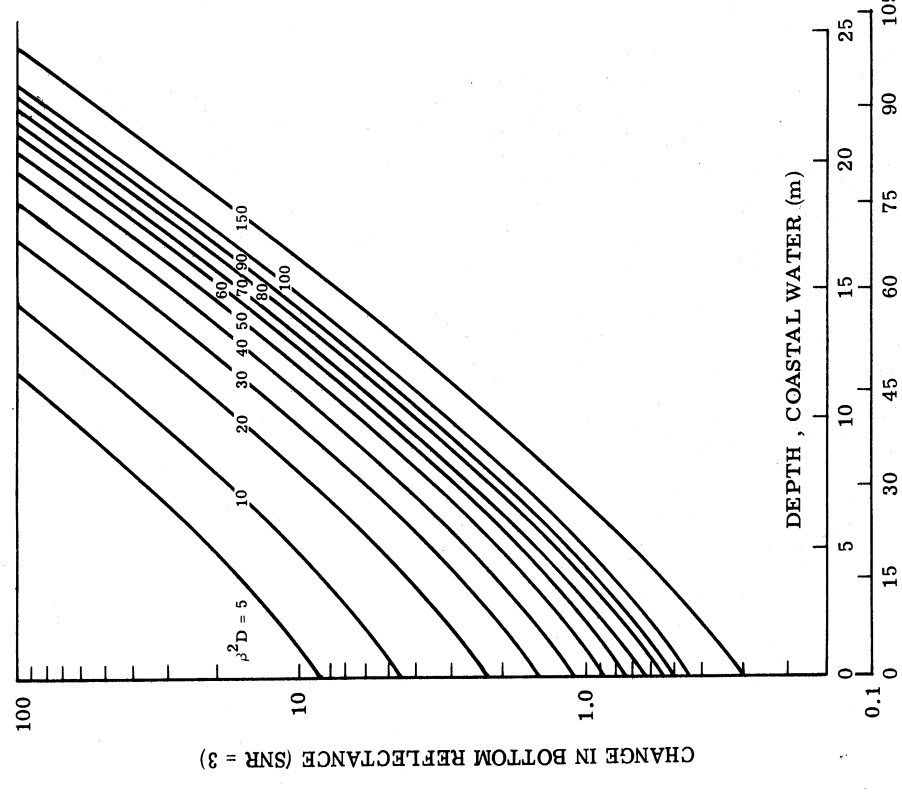

FIGURE 19. PARAMETRIC CURVES RELATING DESIGN, CHANGE IN BOTTOM REFLECTANCE, AND WATER DEPTH FOR THE AIRCRAFT SYSTEM AT 1000 ft. Bright sunlight; $v/h = 0.2\ sec^{-1}$, $\Delta\lambda = 545\text{-}555\ m\mu$; β in mrad, D in cm; S-20 photocathode.

larger-diameter system would be needed; for example, for a 0.2-mrad instantaneous field of view (approximately 240-ft, or 80-m, ground resolution), a diameter of 125 cm would be needed to see the same depths.

5
DETERMINING DEPTH BY WAVELENGTH COMPARISON

5.1. THEORETICAL MODEL

In the linear model, deep-water waves are considered to be simple sine or cosine waves of small amplitude. As a wave moves toward shore, the wave front (the line of the wave crests or troughs) becomes more and more parallel to the contour line of the water depth, and the wave steepness (ratio of wave height to wavelength) changes markedly. In shallow water (a depth of less than one-fourth of the deep-water wavelength), the wavelength decreases, but the wave height increases until the wave train consists of peaked crests separated by the relatively flat troughs. The wave phase-velocity decreases and is also dependent on the depth. During the transformation from deep to shallow water, only the wave period remains essentially constant while all other properties of the wave change.

The wave phase-velocity C is expressed as

$$C^2 = \frac{gL}{2\pi} \tanh \frac{2\pi d}{L} \tag{3}$$

where L is the wavelength, d is the depth of water, and g is the acceleration of gravity. In deep water, $d > L/4$, the phase velocity may be approximated by

$$C_d^2 = \frac{gL_d}{2\pi} \tag{4}$$

where the subscript d denotes deep water. It follows from (3) and (4) that

$$\frac{C^2}{C_d^2} = \frac{L}{L_d} \tanh \frac{2\pi d}{L}$$

Since the period T is essentially constant, and $L = CT$,

$$\frac{C}{C_d} = \frac{L}{L_d} \text{ and therefore } \frac{L}{L_d} = \tanh \frac{2\pi d}{L} \tag{5}$$

But L, as well as d/L, changes with depth, so it is preferable to use d/L_d as a parameter. Since $(d/L)(L/L_d) = d/L_d$, we can write an expression for d/L_d using (5):

$$\frac{d}{L_d} = \frac{d}{L} \tanh \frac{2\pi d}{L}$$

Therefore the wavelength ratios can be plotted as functions of d/L_d by a numerical method, as shown in figure 21.

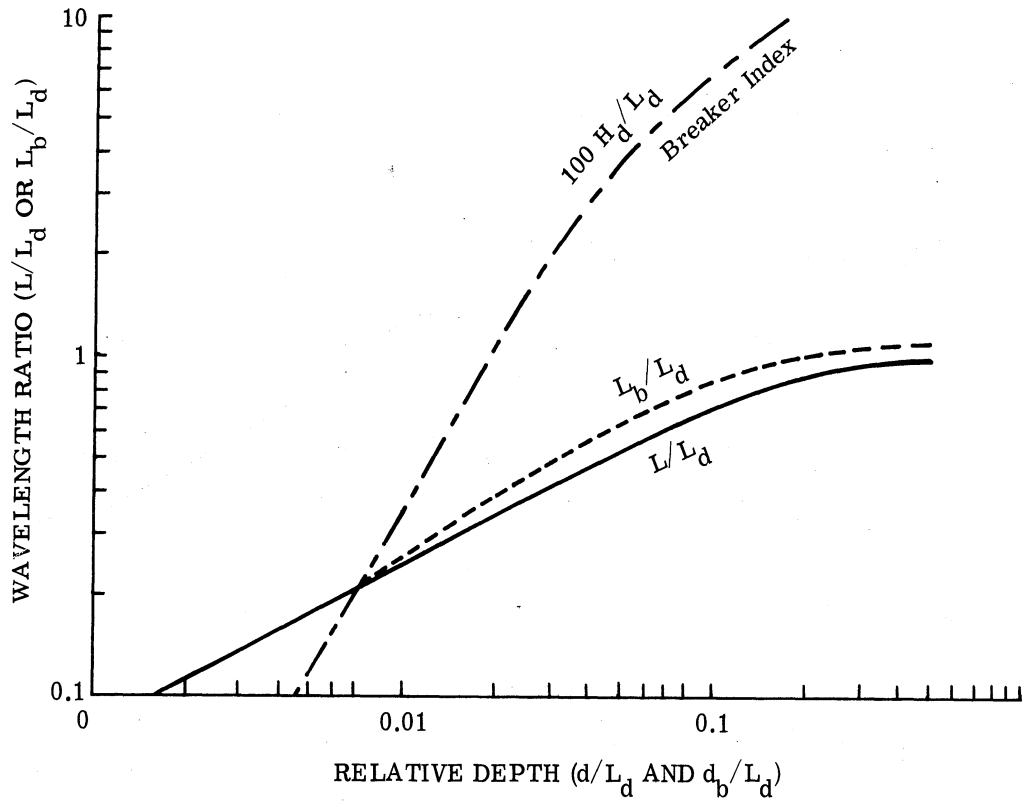

FIGURE 21. WAVELENGTH RATIO VERSUS RELATIVE DEPTH DURING SHOALING

In deep water, a wave becomes unstable and breaks when the forward velocity of the water particle at the top of the crest exceeds the wave velocity. This occurs when the crest angle, which is formed by surface stream lines at the maximum point of the crest, decreases to 120^o (i.e., when the steepness reaches the value of 0.143). Empirical data from observations and experiments have been plotted [43] as initial steepness (d_b/H_b) versus wave-height ratio (H_b/H_d) and versus depth-to-height ratio (d_b/H_d) at the breaking zone. (The subscript b denotes the breaking zone, and H_d is the height of the wave in deep water.) Figure 22 shows six specific wavelength curves plotted as examples of the information in figure 21.

If the deep-water wavelength is measured as L_d = 740 ft, and if the wavelength reduces to L = 330 ft in the direction of wave propagation towards the shore, how can the approximate water depth at this point be calculated? One method would be to use the change-of-wavelength-

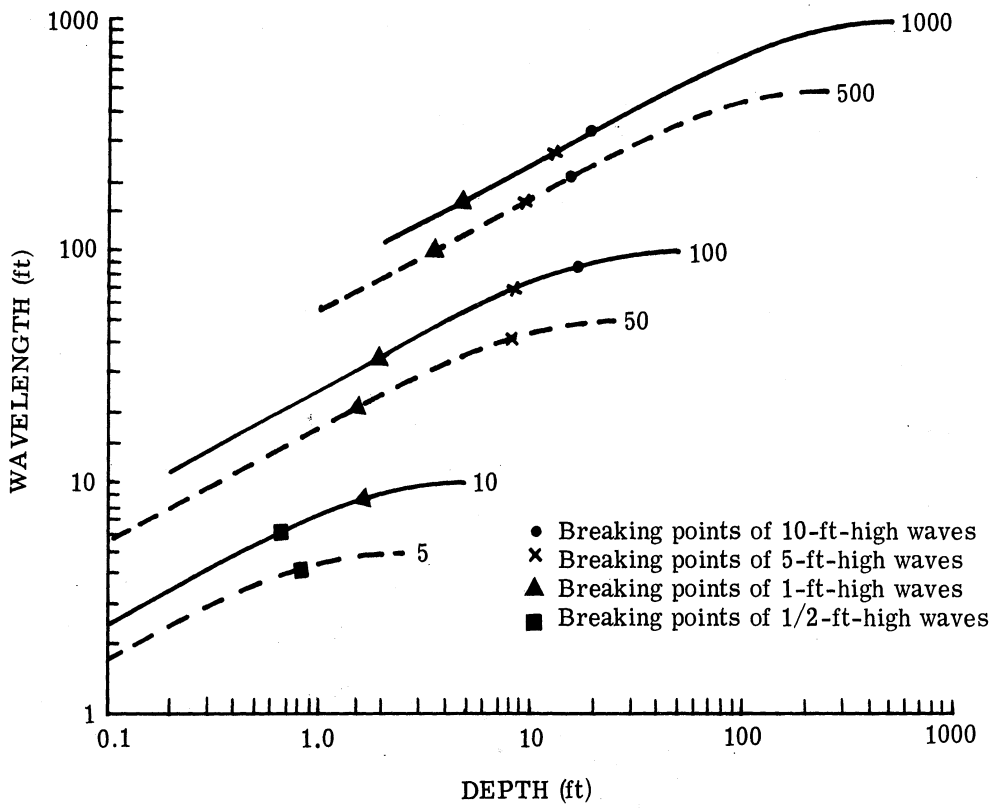

FIGURE 22. WAVELENGTH VERSUS DEPTH DURING SHOALING. Figures beside the curves are the deep-water wavelengths (ft).

versus-relative-depth curve in figure 21. From the wavelength change, we get the wavelength ratio, $L/L_d = 330/740 = 0.446$. Following the curve of L/L_d in figure 21, we get the relative depth ratio from the abscissa, $d/L_d = 0.034$. Therefore at this point, the depth of water should be approximately $d = 0.034L_d$; thus, $d = 0.034 \times 740 = 25.3$ ft. A second method would be to use an interpolation from the wavelength-versus-depth curve (fig. 22). By drawing an approximate curve of $L_d = 740$ ft between curves of $L_d = 1000$ ft and $L_d = 500$ ft and reading at the ordinate a wavelength of L = 330 ft, we find, at the abscissa, the depth d = 25 ft.

If we can quite accurately determine the wavelength as well as the wave height, then from the empirical curve of "breaker index" (fig. 21) we can find the ratio of the depth of the breaking wave to the deep-water wavelength, d_b/L_d, and can thus estimate the breaking depth. Or, from the empirical curve for the ratio of the length of the breaking wave to the deep-water wavelength, L_b/L_d, we can determine this same ratio (d_b/L_d) and thus estimate the breaking depth of the wave. Breaking points of waves 10, 5, 1, and 1/2 ft high are shown by special marks on the curves in figure 22. Sverdrup's [43] empirical and theoretical curves show that long, open-sea waves will become steeper and either decrease in length or break (depending

on the initial height) as they impinge upon shallow water. A special case of this phenomenon is analyzed by Longuet-Higgens [44], who predicts that resonance, or wave trapping, can occur when a given open-sea wave encounters a shoal with a particular geometrical shape.

5.2. DISCUSSION

The practical application of wave-refraction techniques to the detection of shoal waters will depend heavily upon the ability to image surface waves (for wavelength determination) at the research vehicle (aircraft or satellite) and upon use of an optical correlator for wavelength determination. The application of an optical correlator will make it possible to semiautomate the decision process for the detection of shallow waters by using a variable-gate technique to determine the maximum wavelength in the image field. The output from an optical correlator [45] is a diffraction pattern (similar to an X-ray diffraction "powder pattern") that appears as dots in a polar-coordinate field. The dot spacing is dependent on wavelength, and the dot position is related to the azimuth direction of the impinging waves. The dot arrangement is the Fourier transform of the spatial pattern of the waves. (See figure 23 for the optical arrangement for obtaining the Fourier transform. Figure 24 is a conceptualization of the expected transformations for a series of photographs.) Several researchers, such as Stilwell of Naval Research Laboratories,* are attempting to use optical processing to obtain the Fourier transforms of wave patterns in order to acquire sea-state statistics. However, these researchers

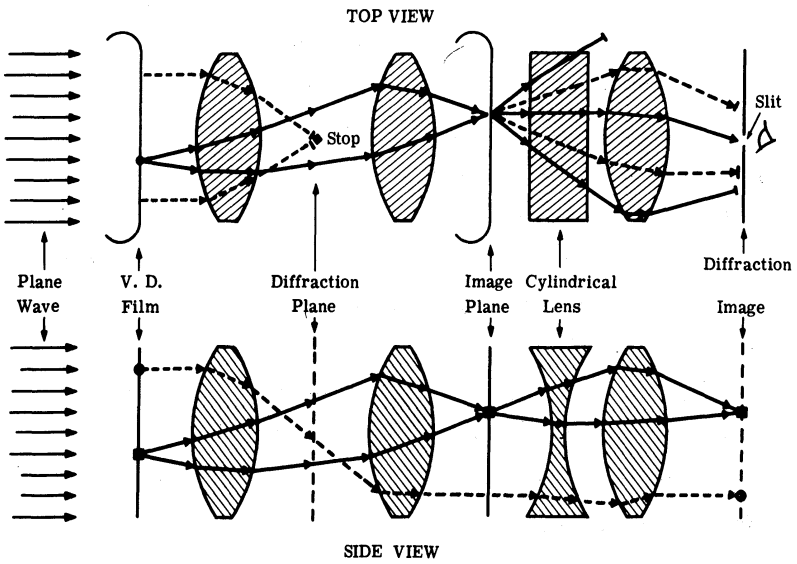

FIGURE 23. SCHEMATIC OF DIFFRACTIVE OPTICAL SYSTEM

*Private communication.

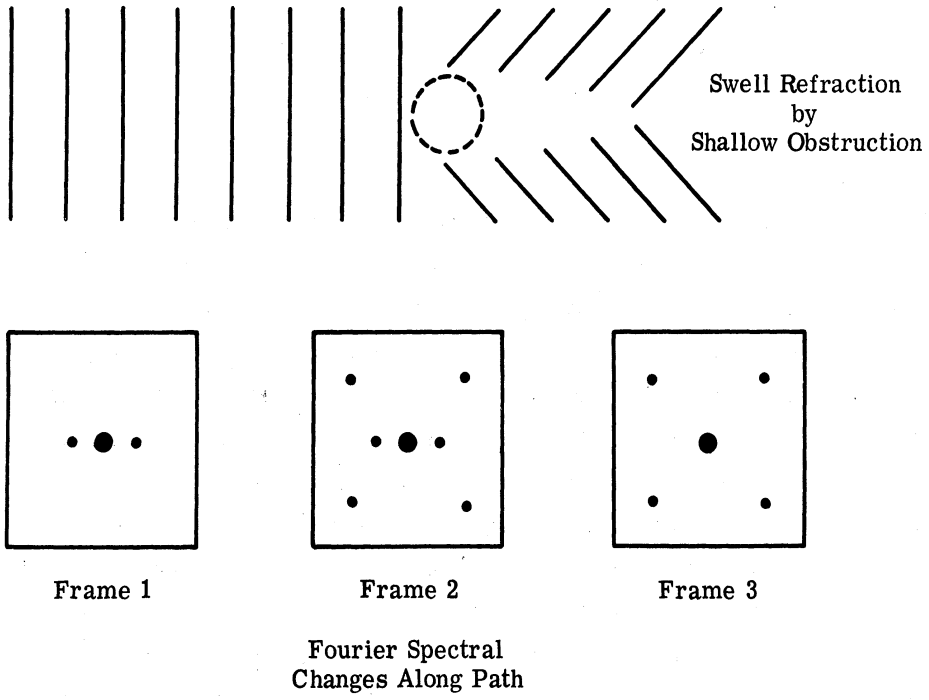

FIGURE 24. CONCEPTUALIZATION OF EXPECTED FOURIER TRANSFORMATIONS ALONG A PATH

are concerned with measuring both wavelength and relative amplitude, based upon the density of the film; this is a very difficult task because it involves the sensitometry of films. Hopefully, the application of wave-refraction techniques to shallow-water location may only require determining whether a particular wavelength is present in one frame and disappears in another. In the optical processor, the Fourier transform plane is photographed, and a wave swell of a given length and direction appears as a point near the center of the transform on the film. The shortest wavelengths appear farthest from the center. The azimuth direction of the pattern is related to the direction of propagation of the wave front. In a preliminary test, a change in the Fourier transform was observed as a result of changes in the wave surface due to the presence of an island (see fig. 25). What is needed now is a series of photographs of wave refraction taken near shallow depths and then optically processed to measure the length of the refracted wave; the best analytical model studies can then be used to estimate water depth from the knowledge of deep-water and refracted wavelength.

The optimum application of the wave-refraction technique depends upon the existence of long plane waves impinging upon a shoal feature. Since these swells are usually generated by storm activities at distances remote from the site of measurement, their form approximates that of plane waves. (Plane waves produce the most distinct "dots" in the optical correlator's

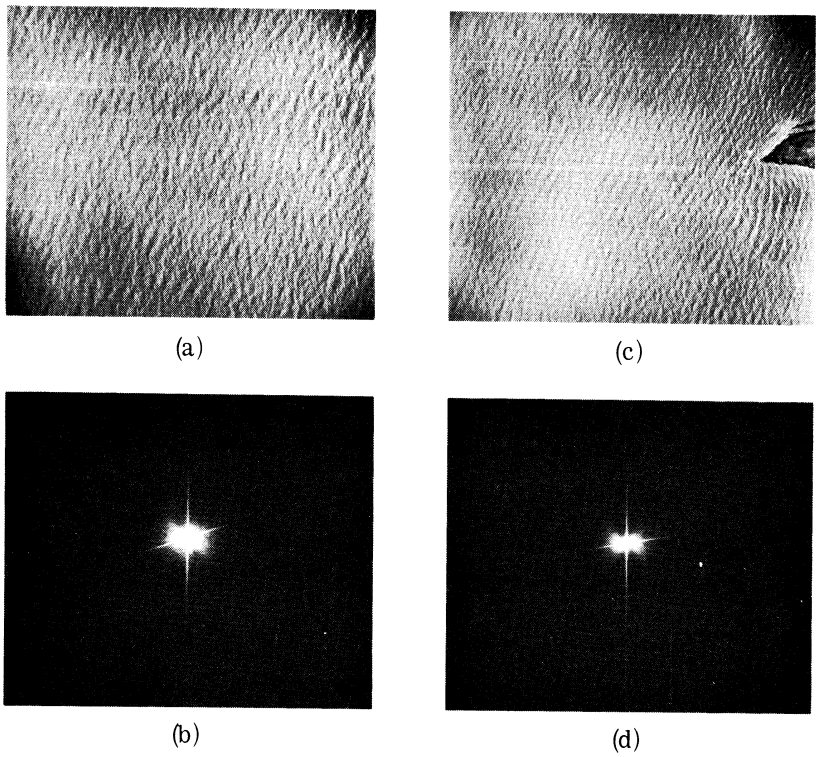

FIGURE 25. PRELIMINARY RESULTS OF OPTICAL PROCESSING SHOWING DIFFERENCES IN FOURIER TRANSFORM DUE TO THE PRESENCE OF AN ISLAND. Parts b and d are the transforms of parts a and c, respectively.

Fourier component pattern.) Open-sea swells range in length from 300 to 800 ft, and occasionally they are as long as 1200 ft. (The record length is up to 5000 ft.) When long waves impinge upon shoal water, they begin to feel bottom and to change their length and/or break. The wavelength change takes place in a manner similar to both the linear-theory wavelength-change curve and the empirical breaking curve given by Sverdrup [43]. From the linear theory, an open-sea wave with a length of 740 ft will reduce to 330 ft when it encounters a depth of 25 ft, if it has not broken by the time it reaches approximately a 50-ft depth, the latter value depending upon the height. Longuet-Higgens [44] shows that a definite short-wavelength resonance may occur when a particular length of open-sea wave encounters either a sea mount or an island shoal of a particular configuration. While the resonance phenomenon is able to provide more exact information than the simple change in length of an open-sea wave, it is expected that the probability of occurrence of resonance will be low, and that it can be considered to be a special case of wavelength change.

The capability of imaging wave patterns is being tested experimentally. Data have been collected in Lake Michigan between 2000 and 12,000 ft, but these have not been analyzed completely. Contrast enhancement of waves is possible through the use of the different polarization properties of reflected sunlight and a changing water-surface slope. Imaging wave patterns by camera or by radar systems from space has one advantage in that the smaller scale leads to a Fourier transform where the longer wavelengths are separated further from the center.

In application, the maximum wavelength within a satellite's image field may be monitored by an optical correlation technique. When waves of lengths greater than 400 ft are indicated, the maximum length will be monitored until a significant reduction of this length is observed in the field. This reduction may take place for any or all of the following reasons: (1) the sensor in orbit may be outrunning the direction of swell propagation from a storm center; (2) the orbit path may be toward the storm center; (3) the wave field may be encountering shoal water. The rate of change of the maximum observed wavelength and direction data from the optical correlator will give information concerning the direction of propagation. If it is suspected that the wavelength change is caused by shoal water, the multispectral "color" record will be examined for a color change, and the thermal record will be examined for a temperature change. Further, the wave record will be examined for direction changes indicating true wave refractions and for wavelength patterns indicating wave trapping of wave energy.

Detection need not be done in real time; multiple passes of a satellite can be used to establish the persistence of color and temperature anomalies and to take advantage of the opportunity to observe the events of wave refraction in the case of swells arriving at the site from several directions.

6
THERMAL ANOMALIES

Of all the observables investigated, the thermal anomaly holds the least promise of positive association with submerged features because of two limiting factors. First, depth of water cannot be inferred from the detection of a thermal anomaly, so the anomaly would be useful only as another indicator of geographical position. Second, there are many other phenomena which affect temperature structure in the oceans (e.g., upwellings, currents, and fronts), so that detection of a thermal anomaly may be a false indication of a hazard to navigation. Nevertheless, a study was made for completeness in an attempt to determine if spatial extent or absolute temperature differences (or anything else) may serve to distinguish types of anomalies and therefore indirectly provide useful information about underwater features. It was encouraging that two examples of infrared thermal imagery show apparent mapping of underwater features due solely to the surface temperature structure. One infrared image, made by HRB-Singer, Inc., shows a length of river, and the thermal variations correspond approximately to depth contours. The other image, obtained by Naval Air Development Center, shows an underwater feature by the variation in the "spatial texture" of the temperature differences at the surface; i.e., one could not find a temperature gradient as such, but one could infer its existence by recognizing a change in the "thermal structure" on the infrared map.

These examples from the "real" world are further supported by a theoretical study by Osborne [46]. Osborne writes an equation for heat balance due to radiation, conduction, and evaporation and thereby expresses radiation temperature in terms of thermal boundary layers in the air and water at the interface. He then calculates the variation in these boundary layers with water and wind velocity and from this determines the expected variation in surface temperature with these velocities. Following are a few significant points made by Osborne:

> (1) The conditions for optimum observation of detailed structure in the sea surface temperature . . . are clear sky, dry air, and especially an appreciable wind. (p. 115)
>
> (2) Slicks would generally be expected to be cold patches. (p. 115)
>
> (3) . . . the stirring of a patch on the water by a subsurface school of fish . . . would appear as a hot patch on the sea . . . by giving . . . a locally decreased water boundary layer thickness . . . a decrease in boundary layer, δ, implies an increase of [temperature] T_o. (p. 122)
>
> (4) . . . air temperature changes, in their effect on changes of T_o, the sea surface temperature, are relative small. (p. 123)
>
> (5) . . . not too much is known experimentally (over the ocean) about boundary layer of air, δ_a, as a function of [wind velocity] U_a, except that it decreases with U_a; that is, $d\delta_a/dU_a$ is negative . . . this is not of much help. Our formula

> tells us we need to know the derivatives especially $\partial\delta_w/\partial(U_w \text{ or } U_a)$. There are no data whatsoever on these points. (p. 123)
>
> (6) The ratio $\lambda = U_w/U_a$ must be small to give detectable signals at ΔT_0 . . . appreciable signals, $\Delta T_0 > 0.1$, are given over a limited range of conditions for λ near zero. (p. 127) [This creates Osborne's choice of "an appreciable wind" but also implies that stationary water will suffice.]
>
> (7) . . . For a case of shallow water in the absence of any confined current, say at the edge of the sea, if there is a tidal current, one can . . . infer that the shallow water appears colder, especially in the presence of wind. In the absence of any current, one might argue (by ignoring wave effects) that the presence of a second boundary (the bottom) close to the surface, would tend to suppress turbulence. This . . . increases the boundary layer thickness, and makes the shallow water colder. (p. 129) [We should note that, given a subsurface current, an abrupt change in depth might, on the contrary, increase turbulence. In any event, a depth change may be manifested in an associated surface temperature change, ΔT_0.]

The important point here is that, although Osborne makes some assumptions which one might argue are unrealistic, there is some justification for arguing a connection between water depth and surface temperature.

The temperature anomaly connection was not found to be related to the heat flow found at the sedimentary bottom of some sea mounts. Birch [47] made measurements of anomalous heat flow through the sediment floor at nine stations near the sea mounts Retriever, Picket, and Balanus in the New England chain. These measurements indicate up to 50% greater flow in certain areas. Birch offers several possible explanations for this higher heat flow but notes that it is impossible at this time to select from these choices, which include, among others, (1) local heat source, (2) rock of higher conductivity, (3) unequal erosion, (4) faulting, (5) radioactivity effects, (6) remnant volcanic action. Of more direct interest to the present problem are the following two statements from Birch: "There is no apparent correlation between heat flow and water depth or proximity to the sea mounts." (p. 5225); and ". . . the absolute temperature readings of the probe did not show any temperature change in the 50 meters above the bottom." (p. 5225) The significant point is that anomolous heating effects do exist and might be detectable as surface effects, especially in the formation of new shoals or islands by volcanic action such as that near the Tonga Islands in the Pacific.

7
LASER DEPTH-RANGING-SYSTEM STUDIES

Water depth appears to be determinable directly by use of an optical laser system which would measure the time difference between the laser-beam reflection from the water surface

and the reflection from the bottom. The signal from the water surface is many times greater than the signal from the bottom because it does not suffer the attenuation losses of the light's double passage through the water medium. Thus it would be required only to investigate the signal-to-noise conditions which influence the signal from the bottom in order to study the maximum depth-ranging capability of laser systems built of state-of-the-art laser components. The range (depth) equation is

$$r = \frac{1}{2\alpha} \ln \underbrace{\left[\frac{P_t \tau_t \tau_r A_r}{(SNR)\left(\frac{2ek^2 \Delta f}{S_c}\right)^{1/2}} \right]}_{\text{Term 1}} \underbrace{\left[\rho_b \tau_a^2 (1 - \rho_w)^2 \right]}_{\text{Term 2}} \underbrace{\frac{\cos \theta}{\pi (h + r)^2}}_{\text{Term 3}} \underbrace{\frac{1}{(P_r + P_{ref} + P_a + P_e + P_d)^{1/2}}}_{\text{Term 4}}$$

Term 1 represents mainly the laser equipment factors; term 2 represents physical factors dependent on water and atmospheric characteristics; term 3 represents mainly the geometric factors such as altitude and angle of incidence; and term 4 represents the signal contribution from the receiver, background, and system noise. The derivation of this equation is presented in the appendix, where the symbols are defined. Because of the potential of the laser ranging system, a thorough tradeoff study for the design parameters was made. The optimum design for laser ranging systems for use from aircraft and spacecraft is given below.

A block diagram of a typical laser ranging system is shown in figure 26. The effects of changes in transmitter peak power (P_t), receiver optical aperture area (A_r), beamwidth (ω_r), and detector (photomultiplier tube) types were studied for three laser systems during both day and night operation. One of these systems was for use in an aircraft at 0.5 km altitude; the other systems, employing scanned lasers to provide additional depth-measuring points for more efficient utilization of a given flight line, were for use in an aircraft at 10 km and in a satellite orbiting at 200 mi. All the systems use Nd^{3+}:glass lasers in some form. Table XI lists the specifications for these systems. It was concluded that a smaller beamwidth would be the best tradeoff in terms of gain, followed by a larger receiver area, more transmitter power, and, finally, cooling of the photomultiplier detector. Weather conditions (i.e., atmospheric conditions) and bottom reflectance effects were also studied. Figures 27 and 28 indicate clearly the effects of cloud layer and fog upon the performance of a laser ranging system in an aircraft (fig. 27) and in a satellite (fig. 28), for day and night operation. The depth (r) is 10 to 20 m for minimum to maximum transmittance of light in coastal waters. Table XII lists all parameter values selected for this study.

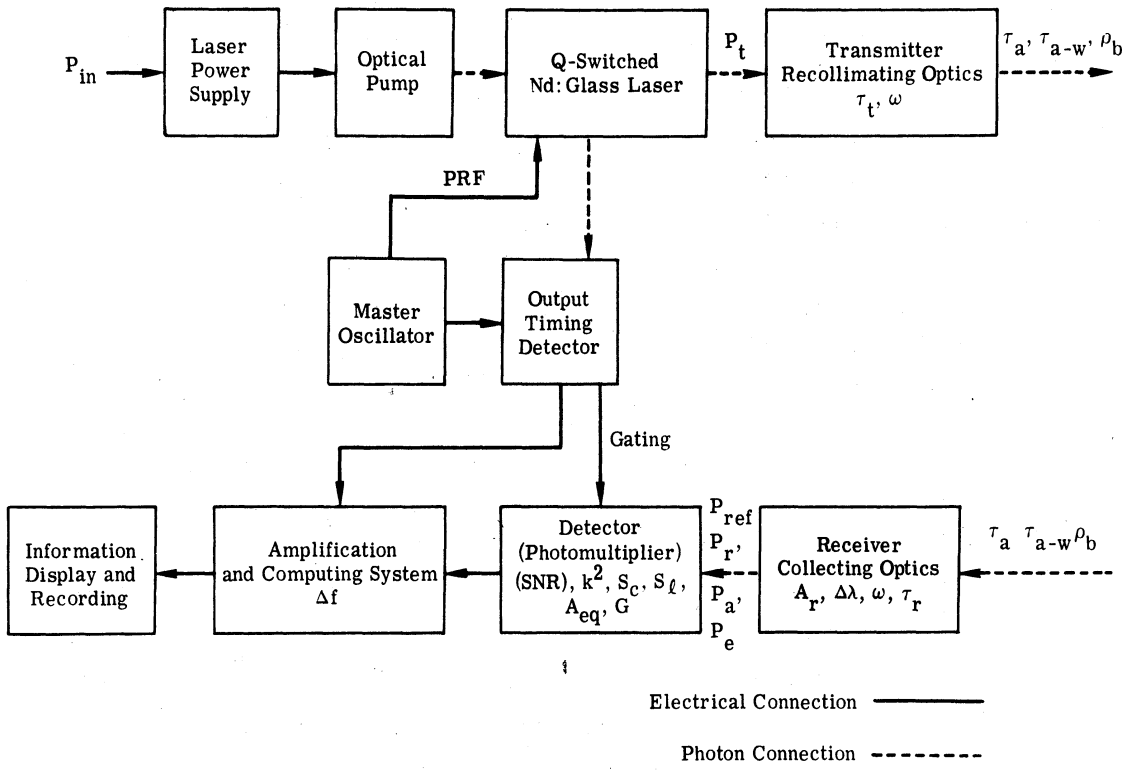

FIGURE 26. BLOCK DIAGRAM OF LASER RANGING SYSTEM (See app. for definition of symbols)

Comparison of tables XI and XII indicates that transmitter peak power has been reduced by using smaller rod diameters and narrower laser-beam divergence, which results in a smaller beamwidth for a constant-diameter optical collimator. This is important for the satellite case because large beamwidths illuminate too large an area, which reduces the resolution and accuracy of the laser ranging system. Also, high peak power with high pulse-repetition frequency (PRF) (high data rates for scanning and for high-speed satellites) requires large prime-power sources and high-capacity cooling systems because laser systems have low efficiency (see table XIII); thus, for high-power output from lasers, the weight of the prime power source and cooling system may be many times the weight of the ranging system. The cooling system for satellites is heavier per kilowatt of input power than that for aircraft, because the heat exchanger for aircraft can use mostly airstream heat transfer, whereas the satellite must use a radiation-type heat exchanger.

The 200-nmi satellite's high velocity (7.4749 km/sec) projected onto the earth with a sector scan causes high data rates which require high PRF and thus high input power (see table XI). Since the velocity of the satellite cannot be changed for a given orbit, the only tradeoffs for a

TABLE XI. OPERATIONAL AND DESIGN PARAMETERS FOR 0.53-μ Nd^{3+}:GLASS LASER RANGING SYSTEM

Operational Conditions	Aircraft Using No Scanning	Aircraft Using Scanning	Satellite Using Scanning
Altitude (m)	h = 500	h = 10^4	h' = 3.704 (10^5)
Platform ground velocity (m/sec)	v = 77.166	v = 61.732	v' = 7.475 (10^3)
Swath width (km)	0	2	10
Data patch spacing* (max) (m)	1	5	20
Illuminated patch diameter	5 cm	1 m	1.852 m
Physical environment			
Atmospheric transmission (Hazy day, sea level attenuation coefficient α = 1 km^{-1})	τ_a = 0.61723	τ_a = 0.28584	τ_a' = 0.27887
Minimum sun angle (zenith)	1/2°	1°	1°
Laser system parameters			
Transmitter			
Type	1-stage laser oscillator	1-stage laser oscillator	2-stage laser oscillator and laser amplifier
Peak power (W)	P_t = 2.5 (10^3)	P_t = 10^6	P_t = (10^4)
Pulse width (nsec)	10	10	1
Pulse-repetition frequency (Hz)	PRF = 77	PRF = 506	PRF' = 3.74 (10^5)
Laser energy output (j)	E_o = 1.925 (10^{-5})	E_o = 5.06	E' = 3.74
Average power output (W)	P_o = 1.925 (10^{-5})	P_o = 5.06	P_o' = 3.74
Power input	P_i = 1.155 W	P_i = 3.03 kW	P_i' = 2.34 kW
Optical system aperture	Refractive, one lens and collimator	Refractive, one lens and collimator	Reflective-refractive, one lens and collimator
Aperture diameter	D_t = 20 cm	D_t = 20 cm	D_t = 1.9 m
Beamwidth (mrad)	ω_t = 2.1	ω_t = 0.1	ω_t = 0.005
Optics transmittance	τ = 0.97	τ = 0.97	τ = 0.97
Receiver			
Type	Pseudo Cassegranian	Pseudo Cassegranian	Pseudo Cassegranian
Optics transmittance	τ = 0.45	τ = 0.45	τ = 0.45
Optical aperture (area)	A_r = 0.5 m^2	A_r = 0.5 m^2	A_r = 0.5 m^2
Beamwidth (mrad)	ω = 0.1	ω = 0.1	ω = 0.005
Optical filter passband	$\Delta\lambda$ = 10 Å	$\Delta\lambda$ = 10 Å	$\Delta\lambda'$ = 0.1 Å**
Signal-to-noise ratio	SNR = 20	SNR = 2	SNR' = 20
Electronic bandpass	Δf = 100 MHz	Δf = 100 MHz	$\Delta f'$ = 1 GHz
Square-law detector	RCA 7029 PM†	RCA 7029 PM	RCA 7029 PM

*Data points are equally spaced across the scan and along the scan track.

**Photomultiplier with S-17 spectral surface operated at 20°C.

† This value can only be obtained by using a grating in the laser cavity.

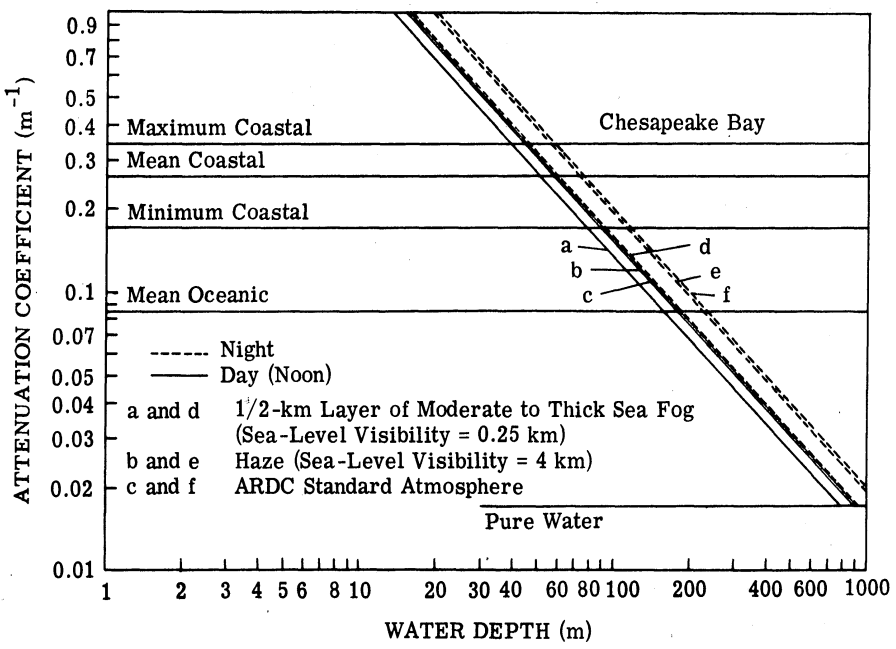

FIGURE 27. EFFECT OF METEOROLOGICAL CONDITIONS ON THE CALCULATED PERFORMANCE OF A LASER RANGING SYSTEM IN AN AIRCRAFT. h = 1/2 km; other parameter values are given in table XI.

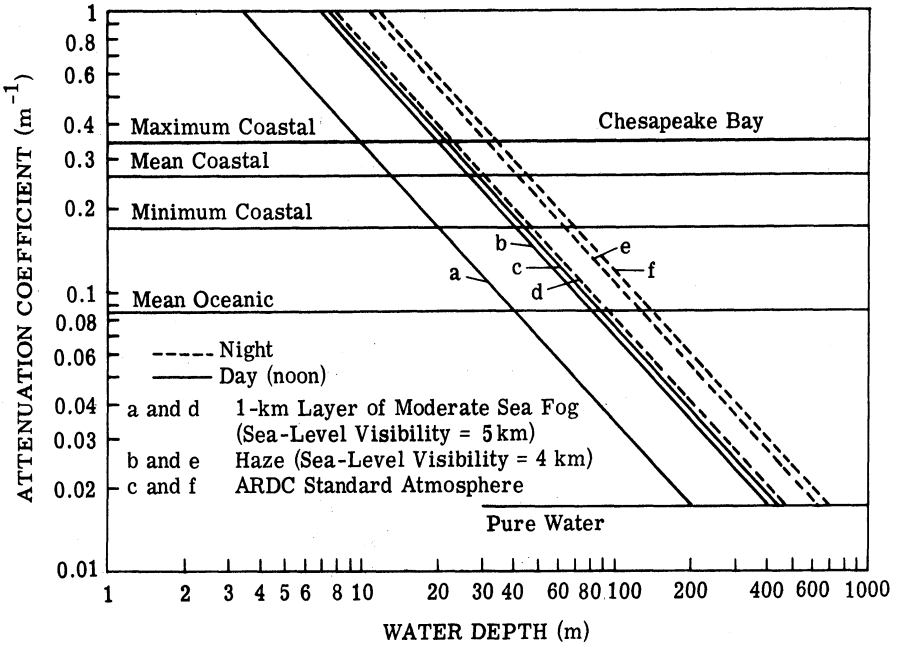

FIGURE 28. EFFECT OF METEOROLOGICAL CONDITIONS ON THE CALCULATED PERFORMANCE OF A LASER RANGING SYSTEM IN A SATELLITE. h = 200 nmi; other parameter values are given in table XI.

TABLE XII. PARAMETER VALUES SELECTED FOR LASER RANGING-SYSTEMS STUDY
(A prime indicates that the value is for the satellite laser system)

System Parameters	
$P_t = P'_t = 2\ (10^8)$ W	Laser transmitter peak power
$\tau_t = \tau_t = 0.97$	Laser transmitter optics transmittance
$\tau_r = 0.45$	Aircraft receiver optics and filter transmittance
$\tau'_r = 0.585$	Satellite receiver optics and grating transmittance
$A_r = A'_r = 1\ m^2$	Area of receiver collecting optics
SNR = SNR' = 20	Signal-to-noise ratio of 13 db
$e = e' = 1.5921\ (10^{-19})$ coulomb	Electronic charge
$\Delta f = \Delta f' = 100$ MHz	Minimum bandwidth for 10-μsec pulse width
$\Delta\lambda = \Delta\lambda' = 10\ \text{Å} = 10^{-3}\ \mu$	Optical filter passband of the receiver
$\omega = \omega' = 1$ mrad	Beamwidth of the transmitter (field of view of the receiver)
$A_{eq} = A'_{eq} = 5\ (10^{-12})$ lm	Equivalent anode dark-current input of an RCA 7029 photomultiplier
$S_l = S'_l = 1.25\ (10^{-6})$ A/lm	Cathode luminous sensitivity of an RCA 7029 photomultiplier
$G = G' = 3.2\ (10^5)$	Tube gain of an RCA 7029 photomultiplier
$S_c = S'_c = 0.085$ A/W	Cathode radiant sensitivity of an RCA 7029 photomultiplier
$k^2 = (k^2)' = 1.4617$	Secondary emission noise factor of an RCA 7029 photomultiplier
Environmental Parameters	
$\tau_a = 0.9330$	Transmittance at 0.53 μ of an ARDC standard atmosphere vertically from sea level to 1/2 km
$\tau'_a = 0.7320$	Transmittance at 0.53 μ of an ARDC standard atmosphere vertically through the total atmosphere to the 200-nmi satellite
$\tau'_{a\text{-}w} = (1 - \rho_\omega) = 0.945$	Average transmittance of water-to-air boundary in which ρ_ω = 0.02 to 0.086 at 0.53 μ with no white caps
$\rho_b = \rho'_b = 0.1$	Reflectance at 0.53 μ of bottom material
$H_{\lambda_w} = 6.7\ (10^1)\ \text{W-m}^{-2}\text{-}\mu^{-1}$	Upward solar irradiance at 0.53 μ off the water surface for high sun angles
$H_{\lambda_a}\ 1.15\ (10^2)\ \text{W-m}^{-2}\text{-}\mu^{-1}$	Upward solar irradiance at 0.53 μ off the atmosphere for high sun angles
$\beta' = 1$	Altitude correction factor for satellite-reflected solar irradiance
$\beta = 0.1929$	Altitude correction factor for aircraft-reflected solar irradiance
$\dfrac{\epsilon_\omega C_1}{\lambda^4 \exp[(C_2/\lambda T) - 1]} < 10^{-35}\ \text{W-m}^{-2}\text{-}\mu^{-1}$	Emitted greybody radiance at 0.53 μ of the ocean surface; negligible compared to solar irradiance reflected off water or atmosphere and to generated noise power (P_d) of the photomultiplier ($P_d = 2.2977\ (10^{-16})$ W)
Operational Parameters	
$h = 5\ (10^2)$ m	Aircraft altitude
$h' = 3.704\ (10^5)$ m	Satellite orbital height (200 nmi)
$\cos\theta_b = 1$	Laser beam normal to water surface and bottom
$\cos\theta_\omega = 1$	Receiver field of view normal to water surface; high sun angle, but receiver does not see specular reflection.

TABLE XIII. CHARACTERISTICS OF HIGH-PEAK-POWER LASERS

Wavelength (μ)	Type	Laser Material	Operating Temperature (^{o}K)	Pump Type	Conventional Mode		Q-Switched Mode						
					Average Output (j)	Efficiency (%)	Output (j)	Peak Power (W)	Pulse Width (nsec)	PRF (Hz)	Efficiency (%)	Line Width (A^{o})	Beamwidth (mrad)
0.3371	Gas	N_2 in air	300^{o}	Plasma discharge			0.1	10^6	4	100	1	0.1	1
0.3472*	Solid state	$Cr^{3+}:Al_2O_3$	300^{o}	Optical	5 (10^2)		75	1 (10^8)	10	100	0.01	0.01‡	1
0.5300*	Solid state	Nd^{3+}:Glass	300^{o}	Optical	10^3	1.2	300	5.6 (10^8)	10		1	50	7.5
0.5300*	Solid state	Nd^{3+}:YAG	300^{o}	Optical	80	4	30	5.6 (10^7)	10	100	1	0.43	1
0.5510 0.5950	Liquid dye	R** in CH_3OH	300^{o}	Nd^{3+} laser			150	2 (10^6)	5	1500	0.036	0.6†	
0.6943	Solid state	$Cr^{3+}:Al_2O_3$	300^{o}	Optical	5 (10^3)	1	15 (10^2)		10	100	0.1	1	2
1.06	Solid state	Nd^{3+}:Glass	300^{o}	Optical	5 (10^3)	3.6	2 (10^3)	10^9	(3-10)	100	0.72		15
1.06	Solid state	Nd^{3+}:Glass	300^{o}	Optical	9.6	6	0.768	8 (10^6)	10	100	1.2		2

*Second harmonic.

**R = rodamine 6G.

†This value can only be obtained by using a grating in the laser cavity.

‡This value can only be obtained by using interference filters.

smaller PRF are fewer data points, larger spacing between data points, or narrower ground swath. The values of PRF, P'_o, and P'_i given for the satellite case in table XI are for data points 20 m apart using a linear scan for a swath 10 km wide, but they would also be correct for a 5-km swath with data points 10 m apart. PRF is proportional to the product of spacing and swath width. For the scan to completely cover the earth's surface for 10-km swaths with the satellite-borne laser ranging system in a 200-nmi polar orbit would require a minimum of 4008 orbits (no overlap), which would take 256.2 days. This swath width, with the same number of data points, is limited by the nadir angle and the wave slope in rough waters of about 16% (the maximum wave slope), so that it would be 0.1437, 2.8675, and 106.21 km for altitudes of 1/2 km, 10 km, and 200-nmi, respectively, for the aircraft- or satellite-borne ranging systems. It should be noted that the depth measurements must be corrected for the change in scan angle and average wave slope of the illuminated area because the laser beam traverses the water at angles other than the vertical, as indicated in figure 29. A maximum off-nadir angle of 16^o plus

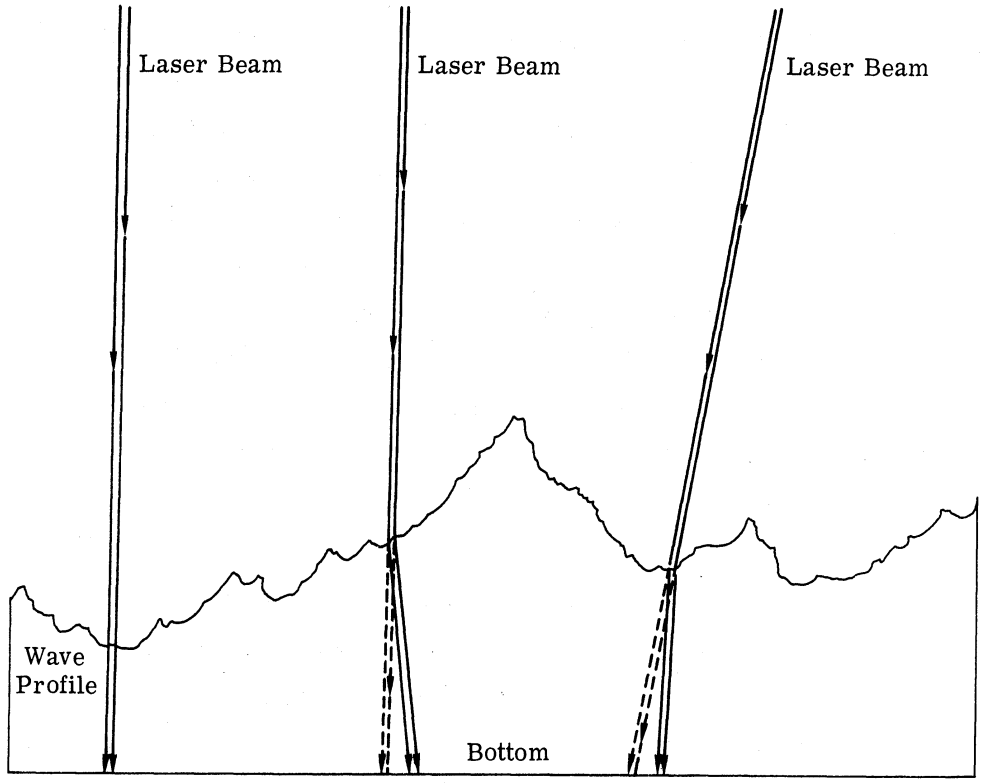

FIGURE 29. ILLUSTRATION OF EFFECT OF WAVE PROFILE ON DEPTH MEASUREMENT

the maximum wave slope of 16^{o} produces a refraction angle of 23.4^{o} by Snell's Law and a path length two and one-half times that of the true vertical-depth path. This indicates that each data point must be corrected, or that we must use a larger number of data points and take the minimum value, which would mean that the wave slope and the laser scan angle are equal and opposite. A larger number of data points across the scan would require a proportionally higher PRF and power input to the laser, which would increase both the power-source and cooling-system weight and volume. This is most critical in satellites and requires trading off to a lower power (less range in the water) for a higher PRF. Note from table XI that both higher power and increased PRF are required at the higher platforms, the 10-km-altitude aircraft and the 200-nmi satellite. The swath width for the aircraft-borne ranging system is angle limited, but the swath width for the satellite-borne system is a tradeoff with peak power, PRF, and pulse width. Note also that the illuminated patch areas of all three laser ranging systems are small compared to the water wavelength for coastal waters.

The physical environment chosen for the system design study was a hazy, cloudless day with the atmosphere having a sea-level attenuation coefficient of $\alpha = 1\ km^{-1}$ (a horizontal visibility of 4 km). For daytime operation, the sun's zenith angle slightly affects the solar radiation reflected from the water (P_{ref}) but doesn't affect the solar radiation reflected from the atmosphere (P_a) for the zenith angles used (up to 5.7^{o} for the 10-km-altitude aircraft laser system). From the tradeoff studies, P_{ref}/P_a was about 10 for the aircraft at 1/2-km altitude, but for the aircraft at 10 km and the 200-nmi satellite, the dominant background was P_a. ($P_a/P_{ref} = 2.36$ for the satellite, and $P_a/P_{ref} = \beta = 2.08$ for the 10-km-altitude aircraft.) The values of P_a and P_{ref} are for the case in which the sun zenith angle is near maximum, except that the solar disc image is not within the receiver beamwidth. For night operation, the optical receiver is limited by detector dark-current-noise power (P_d), and the self-emission power (P_e) of the earth is negligible compared to P_d. It was concluded from the tradeoff studies that cooling of the cathode of the photomultiplier detector is not warranted in the satellite because of the extra weight and because the slight range improvement is only for night operation.

The laser transmitter design (table XI) has been traded off at a lower peak power for the scanning case, where the data rate (PRF) is high. Also, the effect of background has been greatly reduced by use of a very small beamwidth (0.1 and 0.005 mrad for the aircraft and satellite systems, respectively) and very narrow optical filtering (10 and 0.1 Å for the aircraft and satellite systems, respectively). The large-diameter-transmitter optical system is orders of magnitude lighter than a high peak-power tradeoff because of the heavy power sources and laser cooling system required. (Over 99% of the source power generated must be dissipated as heat by the cooling system for the laser rod and optical pump (flash lamp). This requires a

cooling area of about 1 m for radiant cooling per kilowatt plus the two heat exchanges, water, and tubing.) Use of the narrow-passband optical filter (an optical grating) in the satellite system means that a Nd^{+3}:glass laser cannot be used as an oscillator because of its 10-Å line width. Thus it becomes necessary to use a Nd^{3+}:YAG (yttrium-aluminum-garnet) low-power oscillator with a 0.1-Å line width and to amplify the output of the Nd^{3+}:YAG laser with a Nd^{+3}:glass laser (see fig. 30). The required peak-power output of the YAG laser is about 0.01 of the Nd^{3+}:glass laser output, which increases the kilowatt capacity of the power supply and the thermal capacity of the cooling system by only 1%. It should be noted that (comparing tables XI and XII) the transmitter parameters have the greatest change, due to high PRF, P_t, ω_t, Δf, P_i, T (pulse width), and $\Delta\lambda$ tradeoffs. The receiver optical aperture is reduced to 0.5 m^2, but the electronic bandpass for the satellite case is increased from 100 MHz to 1 GHz. (This requires

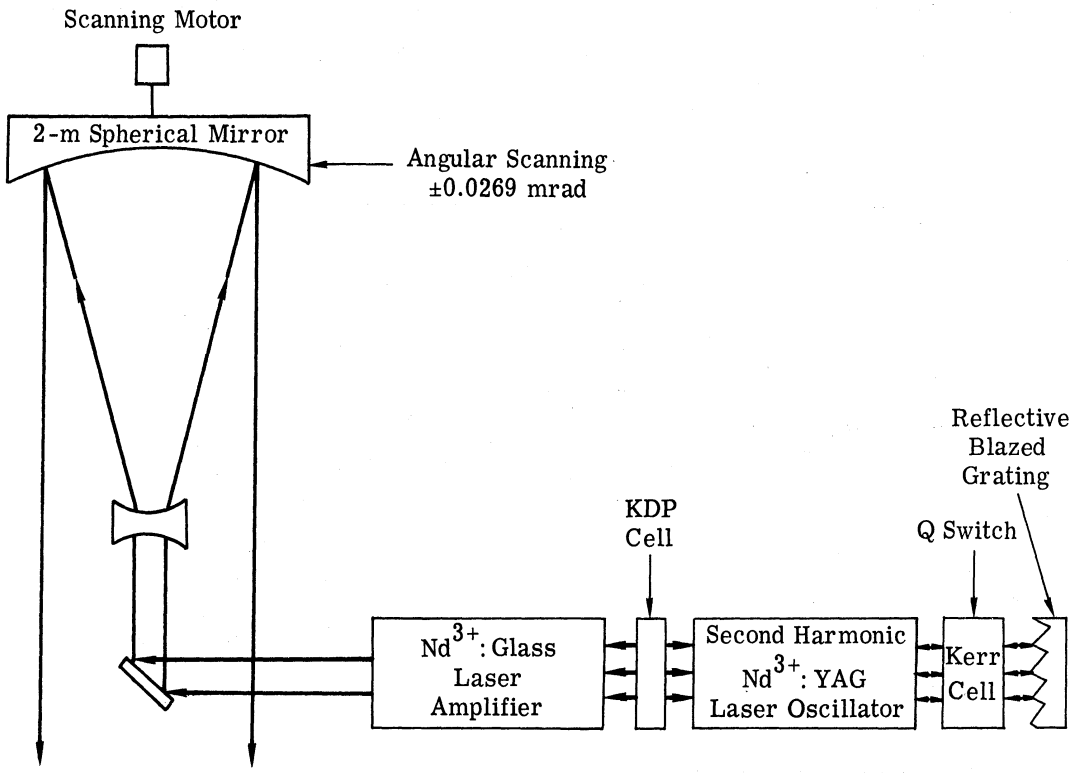

FIGURE 30. SCHEMATIC OF SATELLITE LASER TRANSMITTER. KDP = potassium dihydrogen phosphate.

a traveling-wave tube or high-quality solid-state amplifiers for the satellite.) The receiver optical systems for the satellite and 10-km-altitude aircraft must be totally reflective (mirrors and grating) because of the effect of cosmic rays.

Figure 31 shows plots of laser depth-ranging-system performance using the design parameters from table XI and some of the parameters from table XII. The plot for the satellite system indicates a coastal-waters depth-ranging capability of 15.3 to 30.5 m for daylight conditions (noon) and 15.7 to 31 m for nighttime operation. All the systems show a depth-ranging capability of greater than 10 m for the worst case (maximum attenuation coefficient) of coastal waters; for example, for Chesapeake Bay waters, the satellite system could measure a depth of 15.3 m. For the aircraft system, the coastal waters depth-ranging capability under daylight conditions is 36.5 to 74.0 m at both 1/2 and 10 km altitude. (The system design for 1/2-km-altitude operation was optimized, by reducing the power of the laser, to make the performance equal to that of the 10-km-altitude system.) For nighttime operation, the aircraft depth-ranging capability in coastal waters is 45 to 90 m for the 1/2-km-altitude system and 46 to 93 m for the 10-km-altitude system. The 1/2-km-altitude aircraft operates only along a line track in order to demonstrate the feasibility of the laser ranging system; the 10-km-altitude aircraft and satellite systems are designed for area scanning and require higher data rates. Obviously, better satellite performance would result if there were no scanning.

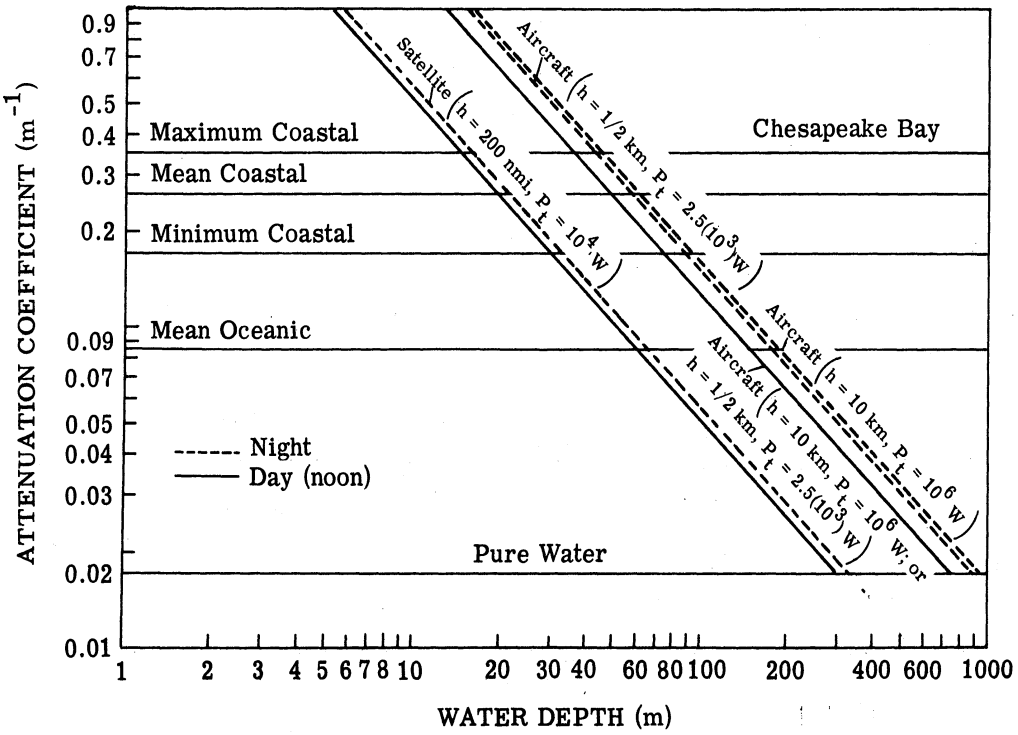

FIGURE 31. PERFORMANCE OF NEODYMIUM LASER RANGING SYSTEMS FROM AIRCRAFT AND SATELLITE PLATFORMS. P_t = peak power; see table XI for other parameter values.

8
CONCLUSIONS AND RECOMMENDATIONS

The following conclusions and recommendations are the result of the investigation of those characteristics associated with shallow water which may be located by remote sensors for use in spacecraft or aircraft.

CONCLUSIONS

(1) All four of the observables considered—color, wave refraction, thermal anomaly, and laser signal return (time difference)—can, under certain conditions, provide information as to the location of shallow-water features.

(2) Only the laser ranging sensor measures depth directly. Tradeoff studies show that presently available components and reasonable system sizes will provide laser systems that can measure depth to 50 m from an aircraft flying at 1/2 km altitude over coastal waters with mean attenuation. However, spacecraft systems tend to be large, so that component and subsystem development must be carried out to assure that these systems are practical in size and reasonable in cost. Design studies show that a laser system with state-of-art components and with a receiver collector area of at least 0.5 m^2 can detect depths to 20 m in coastal waters with mean attenuation. Experimental verification of water-depth measurements with laser systems from aircraft should be made in conjunction with testing of sensor techniques that utilize multispectral data or wave-refraction effects to measure depth. The first opportunity for this will be when the laser systems under procurement by the Naval Oceanographic Office and Naval Air Development Center are available for testing.

(3) First-order theory of wave-refraction effects suggests a method for indicating depth if wavelength change can be measured. To date, only preliminary tests have been performed, making use of the transform plane of the photograph depicting the wave phenomena to measure the wavelength changes. These tests show that a change in the transform does occur, but the change has not yet been quantitatively related to true water depth.

(4) A review of the multispectral scanner electrical output suggests that two or more channels might be used to compute absolute water depth provided that the values of water transmission and bottom reflection were known or could be assumed. The advantages of this approach are in the method of spectral filtering and in the immediate electrical output of the sensor.

RECOMMENDATIONS

(1) Continue use of the thermal infrared sensor in multisensor flight experiments to provide a data base for verifying the presence of thermal anomalies associated with shallow-water features. Under certain conditions, this would support the convergence-of-evidence approach for determining the presence of hazards to navigation, particularly coral reefs and shoals produced by volcanic action. (Coral-reef buildup is restricted to those latitudes where the temperature of the water is at least 68°F.)

(2) Verify sensor characteristics and resolution requirements together with optical processing techniques to quantitatively relate wave-refraction changes to water depth. Determine, if possible, the statistics for swell occurrence and wavelength for areas most likely to contain hazards to navigation.

(3) Verify the accuracy of the method for determining water depth by computation using multispectral scanner data.

(4) Design, build, and flight test laser depth-ranging systems.

(5) Compare wave-refraction, multispectral, and laser techniques in flight to determine their relative accuracy and potential for use from spacecraft altitudes.

(6) Spacecraft experiments can proceed along two paths because of lags in development time: (a) perform initial tests to determine what available cameras, radars, lasers, and scanners systems can do in locating features and measuring depth; (b) conduct second-generation experiments with newly developed sensors designed as a result of recent studies and with sensors being constructed and expected to be ready for use in the 1970-to-1975 time frame.

(7) Generally, the accuracy of depth measurements made with cameras, multispectral scanners, and laser systems will ultimately depend on better knowledge of water transmission and bottom reflection characteristics as a function of geography. Secchi-disk measurements are not accurate enough; spectroradiometric measurements should be carried out. As more photographic and other sensor imagery is made available to aquatic botanists, ecological factors (e.g., plant growth) associated with water depth will be better understood.

(8) Recommended test sites: the southern region of the Gulf of Mexico, for the large number of features for study and discovery; Puerto Rico and other island areas, for better navigation control; certain sea mounts in the northern Pacific, for testing of the capability for geographical location and depth measurement in open waters; the Florida east coast, for navigation control and study of sand and reef type shoals; Lake Michigan, for study of sand and rock type shoals with varying water transmission characteristics; the Grand Bahama Islands, for the best water transmission studies; and, possibly, volcanic shoal areas such as the Tonga Islands, Iceland, or Hawaii.

Appendix
DERIVATION OF A LASER RANGING SYSTEM'S PERFORMANCE

To perdict the performance and/or feasibility of laser ranging systems for water-depth measurements, it is necessary to derive the range equation(s). This equation should take into account the physical and quantum characteristics of the laser transmitter and optical receiver, the attenuation of the laser's electromagnetic radiation in the atmosphere and in sea water, and the spectral reflectance characteristics of coastal waters and ocean bottoms. Also to be considered are the noise limitation due to the background irradiance received by the optical receiver (in this case almost entirely the reflected radiation of sun), the noise generated by the detector (a photomultiplier in this case), and the electronics associated with the quantum detector. The assumption in this derivation is that the transmitter and receiver are mounted coaxially, or adjacent, to each other, and that the bottom of the ocean is a Lambertian reflector while the water surface is a specular reflector with a variable surface profile.

SIGNAL POWER AT THE DETECTOR OF AN OPTICAL RECEIVER

By definition, the power per steradian reflected normal to the surface is P_n, and the power reflected into a solid angle Ω at an angle θ to the normal is

$$P_\Omega = \int_\Omega P_n \cos\theta \, d\Omega \tag{6}$$

$$d\Omega = \sin\theta \, d\theta \, d\phi \tag{7}$$

where ϕ is the azimuthal angle. Combining equations 6 and 7 gives

$$P_\Omega = P_n \iint \cos\theta \sin\theta \, d\theta \, d\phi \tag{8}$$

Integrating over a hemisphere $\left(0 \leq \phi \leq 2\pi, \; 0 \leq \theta \leq \frac{\pi}{2}\right)$ results in the total reflected power, given by

$$P_\pi = P_n \pi \tag{9}$$

But the total reflected power equals $P_i\rho$, where P_i is the total power incident on the target and ρ is the directional reflectance. Therefore,

$$P_n = \frac{P_i \rho}{\pi} \tag{10}$$

Combining equations 6 and 10 gives

$$P_\Omega = \int_\Omega \frac{P_i \rho}{\pi} \cos\theta \, d\Omega \tag{11}$$

but since the receiver's area is small compared to the receiver target range R, $\frac{P_i\rho}{\pi} \cos\theta$ is essentially constant over Ω, and equation 6 becomes

$$P_\Omega = \frac{P_i \rho}{\pi} \Omega \cos\theta \tag{12}$$

Now the total incident power for a beam of uniform power density is related to the transmitted power (P_t) as

$$P_i = P_t \frac{A_t \cos\theta}{A_R} \tag{13}$$

where A_t is the area of the target intercepting the power, θ is the angle between the target normal and the transmitter, and A_R is the normal area illuminated at range R. The solid angle Ω subtended by the receiver is simply

$$\Omega = \frac{A_r}{R^2} \tag{14}$$

Substituting equations 13 and 14 into (12) yields

$$P_\Omega = \frac{\rho A_r P_t A_t \cos^2\theta}{\pi R^2 A_R} \tag{15}$$

When the transmittances of the atmosphere τ_a, the water τ_w, the air-to-water boundary τ_{aw} (i.e., one minus the reflectance of water), the optics of the transmitter τ_t, and the optics of the receiver τ_r are taken in account, the signal power P_r at the detector of the optical receiver is

$$P_r = \frac{\tau_t \tau_r \tau_a^2 \tau_w^2 \tau_{aw}^2 \rho A_r P_t A_t \cos^2\theta}{\pi R^2 A_R} \tag{16}$$

Since the coastal-water bottom is an extended target and intercepts all transmitted energy in the narrow field of view, and assuming that the receiver field of view is boresighted with the transmitter, and that, with near-normal penetration of the water by the laser beam, $A_t \cos\theta = A_R$, equation 16 becomes

$$P_r = \frac{\tau_t \tau_r \tau_a^2 \tau_{aw}^2 \tau_w^2 \rho A_r P_t \cos\theta}{\pi R^2} \tag{17}$$

To determine the received signal power as a function of the water depth r, for the case of an optical radar carried in an aircraft or satellite at altitude h, it becomes necessary to substitute the following equations into equation 17:

$$R = h + r$$

and

$$\tau_w^2 = e^{-2\alpha r}$$

where α is the total attenuation coefficient for the particular coastal waters. Equation 17 becomes

$$e^{2\alpha r} = \frac{\tau_t \tau_r \tau_a^2 \tau_{aw}^2 \rho A_r P_t \cos\theta}{\pi (h + r)^2 P_r} \tag{18}$$

If the range r in water is small compared to the aircraft or satellite height h, then

$$r = \frac{1}{2\alpha} \ln \frac{\tau_t \tau_r \tau_a^2 \tau_{aw}^2 \rho A_r P_t \cos\theta}{\pi h^2 P_r} \tag{19}$$

NOISE CONSIDERATIONS

For night operation, the limiting noise is the noise power P_d generated by the photomultiplier detector. Detection of a signal from the coastal-water bottom will require that

$$P_r > P_d(SNR) \tag{20}$$

where SNR is the signal-to-noise ratio for a given probability of detection and for a given false-alarm rate for a single pulse transmitted and received. The noise power of the detector plus background noise is a limiting condition and will require that

$$P_r > (SNR)(P_d + P_b) \tag{21}$$

where P_b is the power received at the detector from unwanted background radiation. For an aircraft- or satellite-borne laser system, P_b is due to solar reflection off the surface of the water, upwelling from beneath the water, and atmospheric scattering.

SOURCES OF NOISE IN OPTICAL RECEIVERS. The basic noise mechanisms that limit the detecting ability of systems operating in the optical spectrum are Johnson, internal, generation-recombination (G-R), and shot noise.

Johnson noise results from the random motion of charge carriers in a resistive element which generates a random voltage across the element. As the temperature of the resistor is increased, the mean kinetic energy of the carriers increases, yielding an increased electrical noise voltage.

Internal noise consists of dark-current or modulation noise or both, depending on the sensing element used. The modulation noise is characterized by a $1/f^n$ noise-power spectrum, where

n varies from 0.8 to 2. The physical mechanism of this noise is the least understood of all the types of noise.

Generation-recombination noise results from statistical fluctuations in the rate of generation and recombination of charged particles in the sensitive element. The fluctuations can be caused by charge-carrier-phonon interactions or by the random arrival rate of photons from the target and background.

SOURCES OF NOISE IN PHOTOMULTIPLIERS. When a phototube is operated in complete darkness, a small current is noted at the output of the tube. This small dark-current is the result of thermionic emission from the photocathode, leakage currents, corona discharges, fluorescence, and scintillation. The dark current establishes the lower limit on the detectable signal. Being thermionic emission in part, the dark current can be reduced by cooling the phototube. The detector's background current, and even the signal current itself, are statistical and introduce noise into the output.

The statistical emission of electrons at the photomultiplier detector's photocathode, whether due to light inputs or to thermionic currents, gives rise to shot noise. Secondary emission multiplication in the multiplier section of the photodetector contributes some additional noise because of its statistical nature. Therefore, the resulting rms noise current $\left[\overline{i_{on}^2}\right]^{1/2}$ at the output detector is

$$\left[\overline{i_{on}^2}\right]^{1/2} = kK^n\left(\overline{i_{cn}^2}\right)^{1/2} \tag{22}$$

where K is the average gain per stage, and n is the number of stages. The factor k arises from the secondary emission, and i_{cn} is the noise current at the cathode. The factor k is given approximately by

$$k = \left(\frac{K}{K-1}\right)^{1/2} \tag{23}$$

Flicker noise (with a 1/f spectrum characteristic associated with photoemission and with the secondary emission) can be neglected for photomultiplier detectors except at extremely low frequencies (about 1 Hz).

It is convenient to refer the total photomultiplier noise current to the photocathode by dividing equation 22 by the gain of the tube. The result when squared is

$$\overline{i_t^2} = 2eIk^2\,\Delta f \tag{24}$$

where $2eI\Delta f$ has been substituted for $\overline{i_{cn}^2}$ in equation 22, and where e is the electronic charge, Δf is the bandwidth for passing a pulse, I is the average current from all sources, and

$$I = I_b + I_d + I_s \tag{25}$$

Here I_b is the average current due to the background radiation, I_s is the average current due to the signal, and I_d is the average current due to dark current.

BACKGROUND-GENERATED RECEIVER NOISE

The power at the detector which the background sources contribute to the total noise is shown in equations 24 and 25. The sources of this external (background) noise are the solar reflected energy off the surface of the water and the solar reflected energy due to atmospheric scattering. The power reflected per steradian per square cm per micron off the water (smooth water, when the angle of incidence β equals the angle of reflection θ) is

$$N_s = \rho_w N_\lambda \tau_a \tag{26}$$

where ρ_w is the reflectance of the water surface, N_λ is the spectral radiance of the sun, and τ_a is the transmittance of the atmosphere. For the case of rough water, the equation can be modified by a constant:

$$N_s = g\rho_w N_\lambda \tau_a \tag{27}$$

where g is the glint factor, a function of sun zenith angle, ocean roughness, and receiver field of view. The total reflected power on the optical receiver detector is

$$P_{ref} = g\rho_w N_\lambda \frac{\pi\omega^2 R^2 \cos\theta}{4} \frac{A_r}{R^2} \Delta\lambda \tau_a^2 \tau_r \tag{28}$$

where ω is the receiver optical angular field of view (rad), and $\Delta\lambda$ is the passband of the receiver optical system (μ). To reduce the effect of the sun, the optical passband is reduced as much as possible with filters, and all wavelength-dependent parameters can be assumed constant.

Equation 28 reduces to

$$P_{ref} = \frac{\pi g \rho_w \tau_a^2 \tau_r \Delta\lambda \omega^2 A_r N_\lambda \cos\theta}{4} \tag{29}$$

In addition to the sunlight reflected from the water's surface, a portion of the solar radiation is scattered into the receiver from the atmosphere in the field of view of the receiver. The derivation of this solar radiation follows that given in Middleton.* It is assumed that the at-

*W. F. K. Middleton, Vision Through the Atmosphere, University of Toronto Press, 1958, Chapters 6 and 7.

mosphere is uniform and that all parts of the atmosphere within the field of view are equally illuminated. A small cross-sectional element of the cone defined by the receiver's field of view has a volume given by

$$dV = \frac{\pi}{4}(\omega X)^2 dX \tag{30}$$

where X is the distance from the receiver to the circular element of interest. The incremental power scattered per unit path-length per steradian in the direction of the receiver, assuming isotropic scattering, is given by

$$dP_a = \frac{\sigma_s \Delta\lambda H_\lambda (\omega X)^2 dX}{16} \tag{31}$$

where σ_s is the scattering coefficient, and H_λ is the solar irradiance. This power, however, will be reduced by atmospheric absorption and scattering before reaching the receiver. The amount of reduction as a function of X is $e^{-\sigma X}$, where σ is the coefficient of the combined scattering and absorption. The power at the detector is

$$P_a = \frac{\tau_r H_\lambda \Delta\lambda \omega^2 A_r \sigma_s}{16} \int_{h-h'}^{h} e^{-\sigma(X-h+h')} dX = \frac{\tau_r H_\lambda \Delta\lambda \omega^2 A_r \sigma_s}{16\sigma}(1 - e^{-\sigma h'}) \tag{32}$$

where h' is the effective height of the atmosphere for a particular system height h. Since the atmospheric attenuation results almost entirely from scattering, $\sigma \cong \sigma_s$, and

$$P_a = \frac{\tau_r H_\lambda \Delta\lambda \omega^2 A_r}{16}\left(1 - e^{-\sigma_s h'}\right) \tag{33}$$

Another source of background-generated noise is the near-blackbody Planckian emission of water. This power P_e incident on the circular detector is

$$P_e = \frac{\epsilon_w \Delta\lambda \omega^2 A_r \tau_a \tau_r C_1}{4\lambda^5 \exp\left[(C_2/\lambda T) - 1\right]} \tag{34}$$

where ϵ_w = emissivity of water

T = temperature (^oK)

λ = wavelength of interest

$C_1 = 3.74(10^8)$ W-μ^4-m^{-2}

$C_2 = 1.439(10^4)$ μ-^oK

P_e is relatively small, especially at ambient temperatures, for the optical wavelength of system operation and is considered only for completeness.

SNR DERIVATION OF RANGE EQUATION

The SNR, using a photomultiplier detector, is

$$SNR = \frac{P_r}{P_c} \tag{35}$$

where P_r is the effective signal power to a photomultiplier, and P_c is the effective rms noise power to a photocathode:

$$P_c = \frac{\overline{i_{tc}}}{S_c} \tag{36}$$

where $\overline{i_{tc}}$ is the total rms noise current in the photocathode, and S_c is the photomultiplier cathode radiant sensitivity (A/W). The total rms noise current from the photocathode is related to individual rms noise currents as follows:

$$\overline{i_{tc}} = \left(\overline{i}_r^2 + \overline{i}_{ref}^2 + \overline{i}_a^2 + \overline{i}_e^2 + \overline{i}_d^2\right)^{1/2} \tag{37}$$

where subscripts r, ref, a, e, and d refer to noise current due to signal, reflected solar radiation, atmospheric scattering of solar radiation, self emission, and photocathode dark-current, respectively. Substituting equations 24 and 25 into (37), we have the total rms noise current at the photomultiplier:

$$i_t = (2ek^2 \Delta f)^{1/2}(I_r + I_{ref} + I_a + I_e + I_d)^{1/2} \tag{38}$$

where I refers to average current.

The product of the noise current in the photocathode and the tube gain differs from the noise output of the photomultiplier by the k^2 factor, which is due to secondary emission. Also, practical SNR's must take into account the noise of the electronic processing. From equations 36 and 37, the total equivalent noise power P_c becomes

$$P_c = \left(\frac{2ek^2 \Delta f}{S_c}\right)^{1/2} (P_r + P_{ref} + P_a + P_e + P_d)^{1/2} \tag{39}$$

where P_d is the equivalent dark-current power referred to the photocathode, and

$$P_d = \frac{A_{eq}}{G}\frac{S_\ell}{S_c}$$

where A_{eq} = anode equivalent dark-current (lm)

G = gain of the tube

S_ℓ = luminous sensitivity (A/lm)

Thus, the SNR for the system is the received signal power P_r (eq. 18) divided by the equivalent noise-generated powers of the detector:

$$\text{SNR} = \frac{P_t e^{-2\alpha r} \tau_t \tau_r \tau_a^2 \tau_{aw}^2 \rho A_r \cos\theta \left(S_c^{1/2}\right)}{\pi(h+r)^2 (2k^2 e\,\Delta f)^{1/2} (P_r + P_{ref} + P_a + P_e + P_d)^{1/2}} \tag{40}$$

For night operation, P_{ref} and P_a would become very small and could be neglected. For daytime operation, P_{ref} and P_a will dominate, and P_e and P_d can be neglected. When h becomes large compared to r (for the case of a satellite), the $(h + r)^2$ term can set to h^2. Equation 40 written in terms of the variables r and α is

$$\alpha r = \frac{1}{2} \ln \frac{P_t \tau_t \tau_r \tau_a^2 \tau_{aw}^2 \rho A_r S_c^{1/2} \cos\theta}{\pi(h+r)^2 (\text{SNR})(2ek^2\,\Delta f)^{1/2} (P_r + P_{ref} + P_a + P_e + P_d)^{1/2}} \tag{41}$$

where r = depth of water

α = extinction coefficient of water

P_t = transmitter power

τ_t = transmittance of transmitter optics

τ_r = transmittance of receiver optics

τ_a = transmittance of air

τ_{aw} = one minus reflectance of water

ρ = reflectance of ocean bottom

A_r = area of receiver collector

S_c = photomultiplier cathode sensitivity (A/W)

θ = angle between transmitter axis and water surface normal

h = height of aircraft or spacecraft

SNR = signal-to-noise ratio

e = electronic charge

k = secondary emission factor

Δf = electrical bandwidth

P_r = received signal power

P_{ref} = noise-equivalent power from water reflection

P_a = noise-equivalent power from atmospheric scattering

P_e = noise-equivalent power from emission of background

P_d = noise-equivalent power from detector

REFERENCES

1. "Doubtful Hydrographic Data, Part A, North Atlantic Ocean," International Hydrographic Bureau Special Publication No. 20, 3rd ed., Monaco, 1967.
2. J. G. Gilg and J. J. McConnel, Jr., "Non-Existent Seamounts—A Case Study," Informal Manuscript No. IM66-28, U. S. Naval Oceanographic Office, Washington, D. C., September 1966.
3. 47th Handbook of Chemistry and Physics, The Chemical Rubber Co., Cleveland, 1966.
4. G. Neuman and W. L. Pierson, Jr., Principles of Physical Oceanography, Prentice-Hall, 1966, chap. 3.
5. Handbook of Geophysical and Space Environments, ed. by S. L. Valley, McGraw-Hill, 1965, chap. 7.
6. E. Ornstein, Attenuation of Electromagnetic Radiation by Sea Water, Report No. 5280, Naval Research Laboratories, Washington, D. C., April 1959.
7. F. S. Brackett, "Chart Measurement and Application of Visible and Near Visible Radiation," Biological Effects of Radiation, Vol. 2, ed. by B. M. Duggar, McGraw-Hill, 1936.
8. Y. LeGrand, "The Penetration of Light Into the Sea," Annales l' Inst. Oceanogr., Vol. 19, No. 1, 1939, pp. 393-436.
9. W. R. Sawyer, "The Spectral Absorption of Light by Pure Water and Bay of Fundy Waters," Contrib. Canadian Biology and Fisheries, New Series, Vol. 7, No. 8, p. 73.
10. N. G. Jerlov, "Optical Studies of Ocean Waters," Rept. of the Swedish Diep. Exp., Vol. 3, No. 1, 1951, pp. 3-51.
11. R. A. Oster and G. L. Clarke, "The Penetration of the Red, Green, and Violet Components of Daylight into Atlantic Waters," J. Opt. Soc. Am., Vol. 25, No. 3, 1935, pp. 84-91.
12. S. Q. Duntley, "Light in the Sea," Journal Opt. Soc. Am., Vol. 53, No. 2, 1963, pp. 214-233.
13. C. L. Utterback, "Spectral Bands of Submarine Solar Radiation in the North Pacific and Adjacent Waters," Conseil Perm. Intern. p l' Expl. do la Mer Rapp et Proc.-Verb. (Denmark), Vol. 101, Part 2, No. 4, 1936, pp. 1-13.
14. J. R. Collins, "Change in Infrared Absorption Spectrum of Waters with Temperature," Phys. Rev., Vol. 26, p. 771.
15. S. A. Sullivan, "Experimental Study of the Absorption in Distilled Water, Artificial Sea Water, and Heavy Water in the Visible Region of the Spectrum," J. Opt. Soc. Am., Vol. 53, No. 8, 1963, pp. 912-968.
16. G. L. Clarke, "Laboratory Analysis of the Selective Absorption of Light by Sea Water," J. Opt. Soc. Am., Vol. 29, No. 2, 1939, pp. 43-55.
17. L. F. Small and H. Curl, Jr., "The Relative Contribution of Particulate Chlorophyll and River Tripton to the Extinction of Light off the Coast of Oregon," Limnology and Oceanography, Vol. 13, No. 1, pp. 84-91.
18. G. A. Riley, "Oceanography of Long Island Sound, 1952-1954II," Physical Oceanography Bulletin, Bingham Oceanography Collection, Vol. 15, pp. 15-46.

19. C. S. Yentsch, "The Influence of Phytoplankton Pigments on the Color of Water," Deep-Sea Research (U.K.), Vol. 7, No. 1, 1959, pp. 1-9.

20. J. E. Tyler, "In Situ Spectroscopy in Ocean and Lake Waters," J. Opt. Soc. Am., Vol. 55, No. 7, 1965, pp. 800-805.

21. H. H. Poole and W. R. G. Atkins, "Photo-Electric Measurements of Submarine Illumination Throughout the Year," J. Marine Biol. Assn. (U.K.), Vol. 16, 1929, pp. 297-329.

22. L. K. Lepley, "Coastal Water Clarity from Space Photographs," Photogrammetric Eng., Vol. 34, No. 7, 1968, pp. 667-674.

23. J. R. Lewis, "The Mode of Occurrence of the Universal Intertidal Zones in Great Britain," J. Ecol., Vol. 43, 1955, pp. 270-290.

24. T. Levring, "Submarine Light and Algal Shore Zonation," Light as an Ecological Factor (Symposium No. 6 of the British Ecological Society), ed. by R. Bainbridge, G. Evans, and O. Rackham, Blackwell, 1966, pp. 305-318.

25. G. Berthold, "Uber die Verteilung der Algen im Golf von Neapel nebst einem Verzeichnis der bisher daselbst beobachteten Arten," Mitt. zool. Stn. Neapel, Vol. 3, 1882, pp. 393-536.

26. J. Feldman, "Ecology of Marine Algae," chap. 16 in Manual of Phycology, ed. by G. M. Smith, Chronica Botanica, 1951.

27. L. D. Druehl, "Distribution of Two Species of Laminaria as Related to Some Environmental Factors," J. Phy., Vol. 3, 1967, pp. 103-108.

28. T. A. Stephenson and A. Stephenson, "Life Between Tide Marks in North America, I: The Florida Keys," J. Ecol., Vol. 38, No. 2, 1950, pp. 354-402.

29. J. M. Kain, "A Study on the Ecology of Laminaria Hyperborea," IVth Congress Intern. Algues Marine, 1961, pp. 207-214.

30. I. Jorde and N. Klavestad, "The Natural History of the Hardangerfjord: Part 4, The Benthonic Algal Vegetation," Sarsia (Norway), Vol. 9, pp. 1-99.

31. G. R. Forster, "Underwater Observations on Rocks Off Stoke Point and Dartmouth," J. Mar. Biol. Assn. (U.K.), Vol. 34, 1955, pp. 197-199.

32. J. M. Kain, "Direct Observations on some Manx Sublittoral Algae," J. Marine Biol. Assn. (U.K.), Vol. 39, 1960, pp. 609-630.

33. J. A. Kitching, "Studies in Sublittoral Ecology III, Laminaria Forest on the West Coast of Scotland," Biol. Bull., Vol. 30, 1941, pp. 324-337.

34. F. T. Walker, "Sublittoral Seaweed Survey of the Orkney Islands," J. Ecol., Vol. 38, 1950, pp. 139-165.

35. C. I. MacFarlane, "Studies in Seaweed Populations of Economic Importance in Digby Neck Area, Nova Scotia," 2nd International Seaweed Symposium, Trondheim, 1955.

36. L. H. Colinvaux, "Distribution of Marine Algae in the Bay of Fundy, N. B., Canada," 5th International Seaweed Symposium, 1965, pp. 91-98.

37. A. A. Aleem, "A Quantitative Study of the Benthic Communities Inhabiting the Kelp Beds off the California Coast," 2nd International Seaweed Symposium, Trondheim, 1955.

38. H. L. Andrews, "The Kelp Beds of the Monterey Region," J. Ecol., Vol. 26, 1945, p. 24.

39. J. H. McLean, "Sublittoral Ecology of Kelp Beds of the Open Coast Near Carmel, California," Biol. Bull., Vol. 122, 1962, pp. 95-114.

40. M. Neushul, "Scuba Diving Studies of the Vertical Distribution of Benthic Marine Plants," Proc. Fifth Marine Biol. Symp., Goteborg, 1964.

41. M. S. Doty, "Rocky Intertidal Surfaces," Mem. Geol. Soc. Am., Vol. 67, Part 1, 1957, pp. 535-585.

42. F. Thomson, A Simple Spectral Discrimination Technique for Target Recognition (U), Report No. 6400-118-T, Willow Run Laboratories of the Institute of Science and Technology, The University of Michigan, Ann Arbor, September 1967 (CONFIDENTIAL).

43. H. V. Sverdrup, M. W. Johnson, and R. H. Fleming, The Oceans — Their Physics, Chemistry and General Biology, Prentice Hall, 1964, chap. 3.

44. M. S. Longuet-Higgens, "On the Trapping of Wave Energy Around Islands," J. Fluid Mech., Vol. 29, No. 4, pp. 781-821.

45. P. Jackson, "Diffractive Processing of Geophysical Data," Appl. Opt., Vol. 4, No. 4, 1965, pp. 419-427.

46. M. F. M. Osborne, "The Interpretation of Infrared Radiation from the Sea in Terms of Its Boundary Layer," Deutsche Hydrographiche Zietschrift, Vol. 17, No. 3, 1964, pp. 115-136.

47. F. S. Birch, "Heat Flow Near the New England Seamounts," J. Geophys. Res., Vol. 70, No. 20, 1965, pp. 5223-5226.

DISTRIBUTION LIST

National Aeronautics and Space Administration
Office of Space Science and Applications
Washington, D. C. 20546

ATTN: Code SAR (3)

Mr. Norman Foster, Manager
Earth Resources Aircraft Program
Code TF-2
NASA Manned Spacecraft Center
Houston, Texas 77058 (1)

Mr. Jim Morrison
Code I
NASA Headquarters
Washington, D. C. 20546 (1)

Mr. Frank Goodson
Code BM-5
NASA Manned Spacecraft Center
Houston, Texas 77058 (5)

Mr. Sid Whitley
Data Manager, Mission and Data Planning Center
Code TF-2
NASA Manned Spacecraft Center
Houston, Texas 77058 (5)

Project Manager
Spacecraft Oceanography Project
Naval Oceanographic Office
c/o Naval Research Laboratory
Building 58, Room 205
Washington, D. C. 20390 (25)

Dr. Charles L. Osterberg
Marine Biologist
Environmental Sciences Branch
Division of Biology and Medicine
Atomic Energy Commission
Washington, D. C. 20545 (1)

Dr. Paul M Maughan
Special Assistant to the Assistant
Director for Biological Research
Bureau of Commercial Fisheries
Department of the Interior
18th and C Street, N. W.
Washington, D. C. 20240 (1)

Mr. Duane G. Robbins
Naval Air Systems Command
Code AIR 53831
Department of the Navy
Washington, D. C. 20360 (1)

Frank J. Silva, Dept. of Health, Education and Welfare
Room 320, Woodmont Building
8120 Woodmont Avenue
Bethesda, Maryland 20014 (1)

Mr. John E. McLean
Operations Officer, Water Resources Studies
Department of the Interior
Room 1006, Indiana Building
633 Indiana Avenue, N.W.
Washington, D. C. 20201 (1)

Mr. Robert W. Popham
National Environmental Satellite Center
Department of Commerce, Code S.2
FOB #4, Room 0226
Washington, D. C. 20233 (1)

Dr. Joshua I. Tracey, Deputy Chief
Office of Marine Geology and Hydrology
U. S. Geological Survey
Department of the Interior
Room 4225, GSA Building
Washington, D. C. 20242 (1)

Dr. William B. McLean
Technical Director (Code 01)
Naval Undersea Warfare Center
San Diego, California 92152 (1)

Dr. S. Russell Keim, Executive Secretary
Committee on Ocean Engineering
National Academy of Engineering
2101 Constitution Avenue, N.W.
Washington, D. C. 20418 (1)

Dr. Gifford C. Ewing
Woods Hole Oceanographic Institution
Woods Hole, Massachusetts 02543 (1)

Professor John D. Isaacs
Scripps Institution of Oceanography
University of California
La Jolla, California 92106 (1)

Officer in Charge
Navy Space Systems Activity
Headquarters Space Systems Division
Air Force Unit Post Office
Los Angeles, California 90045 (1)

Dr. William E. Benson
Head, Earth Sciences Section
Division of Environmental Sciences
National Science Foundation
1800 G. Street, N.W.
Washington, D. C. 20550 (1)

Commander David D. Heerwagen, USN
Office of Naval Research
Code 461-Air Programs Branch
Department of Navy
Washington, D. C. 20360 (1)

Dr. Sidney R. Galler
Assistant Secretary of Science
Smithsonian Institution
Room 213
10th and Jefferson Drive. N.W.
Washington, D. C. 20560 (1)

Mr. Thorndike Saville, Jr.
Chief, Research Division
U. S. Army Coastal Engineering
Research Center
5201 Little Falls Road, N.W.
Washington, D. C. 20016 (1)

Mr. Amborse O. Poulin
U. S. Army Cold Regions Research and
Engineering Laboratory
P. O. Box 282
Hanover, New Hampshire 03755 (1)

Commander Robertson P. Dinsmore
Commanding Officer
U. S. Coast Guard Oceanographic Unit
U. S. Coast Guard
Building 159-E, Washington Navy Yard Annex
Washington, D. C. 20390 (1)

Dr. Wayne C. Hall
Associate Director of Research
Code 7000
Naval Research Laboratory
Washington, D. C. 20390 (1)

Dr. Ronald J. P. Lyon
Chairman, Infrared Team
Geophysics Department
Stanford University
Palo Alto, California 94305 (1)

Dr. Richard K. Moore
University of Kansas
Center of Research in Engineering Science
Lawrence, Kansas 66044 (1)

Dr. Frank T. Barath
183-701
Jet Propulsion Laboratory
California Institute of Technology
4800 Oak Grove Drive
Pasadena, California 91103 (1)

Mr. William R. Hemphill
Room 1123, Crystal Plaza
2221 Jefferson Davis Highway
Arlington, Virginia 22202 (1)

Dr. William T. Pecora, Director
U. S. Geological Survey
Department of Interior
GSA Building
Washington, D. C. 20240 (2)

Dr. Arch Park
Agricultural Research Service O.A.
U. S. Department of Agriculture
Washington, D. C. 20250 (2)

Commander
U. S. Naval Oceanographic Office
Washington, D. C. 20390
ATTN: Library (Code 1640) (3)

Defense Documentation Center
Cameron Station
Alexandria, Virginia 22313 (10)

Dr. James Zaitzeff
NAVOCEANO Liaison Scientist
Code TF
NASA Manned Spacecraft Center
Houston, Texas 77058 (1)

Dr. Joseph Lintz, Jr.
Geology-Geography Department
Mackay School of Mines
University of Nevada
Reno, Nevada 89507 (1)

Mr. Feenan D. Jennings
Physical Oceanography Programs
Ocean Science and Technology Group
Naval Research Laboratory
Code: 408/416
Washington, D. C. 20360 (6)

Ing. Victor Dezerega
Seccion Meteorologia
Universidad de Chile
Cassilla 2777
Santiago, Chile (1)

Dr. Charles C. Bates
Office of the Commandant
U. S. Coast Guard
1300 E Street, N.W.
Washington, D. C. 20591 (1)

Dr. Jack Conaway
Planetary Radiations Branch
Goddard Space Flight Center
Greenbelt, Maryland 20771 (1)

Department of Oceanography
University of Hawaii
Honolulu, Hawaii 96822 (1)

Head, Department of Oceanography
Florida State University
Tallahassee, Florida 32306 (1)

Dr. Dewitt C. Van Siclen, Chairman
Department of Geology
University of Houston
Houston, Texas 77004 (1)

Dr. John A. Knauss, Dean
Graduate School of Oceanography
University of Rhode Island
Kingston, Rhode Island 02881 (1)

Dr. D. E. Wohlschlag, Director
The University of Texas
Marine Sciences Institute
Port Aransas, Texas 78373 (1)

Dr. Robert A. Ragotzkie
Department of Meteorology
University of Wisconsin
Madison, Wisconsin 53706 (1)

Mr. Al Conrod
Experimental Astronomy Laboratory
Building N51-311
265 Massachusetts Avenue
Massachusetts Institute of Technology
Cambridge, Massachusetts 02139 (1)

Director
Lamont Geological Observatory
Columbia University
Palisades, New York 92038 (1)

Dr. C. Rooth
Institute of Atmospheric Science
Computer Center
University of Miami
Coral Gables, Florida 33124 (1)

Dr. Robert E. Stevenson
Bureau of Commercial Fisheries
Biological Laboratory
Fort Crockett
Galveston, Texas 77550 (1)

A. R. Barringer Research Ltd.
304 Carlingview Drive
Rexdale, Ontario, Canada (1)

Dr. E. D. McAlister
Applied Oceanographic Group
Scripps Institution of Oceanography
La Jolla, California 92038 (1)

Head
Department of Coastal Engineering
University of Florida
Gainesville, Florida 32601 (1)

International Hydrographic Bureau
Avenue President J. F. Kennedy
Monte Carlo
Principality of Monaco (1)

Capt. W. Mackinley
Servicio de Meteorologia Maritima
Servicio de Hidrografia Naval
Avenida Montes de Oca 2124
Buenos Aires, Argentina, S. America (1)

Jose M. Rivas S.
Dirección General de Faros e
Hidrografia (Oceanografia)
Ave Coyoacan #131
Mexico 12, D.F. (1)

Ing. Guillermo P. Salas
Director Del Instituto de Geologia
CD. Universitaria
Mexico 20, D.F. (1)

Lt. Alberto M. Vasquez
Euskaro #30
Mexico 14, D.F.
Mexico (1)

Secretaria de Recursos Hidraulicos
Ing. Fortunato Martinez Farias
Dirección Gral. de Plaueacion
Reforma 69-12º Piso
Mexico, D.F. (1)

Lic. Carlos Elizondo
Secretaria Particular de Communicaciones
Centro SCOP
Mexico, D.F. (1)

Ing. Hector Alonso
Rodano No. 14 - 1er Piso
Comision Federal de Electricidad
Mexico 5, D.F. (1)

Sevicio de Hidrografia Naval
Departamento de Oceanografia
Avenida Montes de Oca 2124
Buenos Aires, Argentina, South America (1)

Mr. Affonso da S. Mascarenhas, Jr.
Instituto Oceanografico da
Universidade de Sao Paulo
Caixa Postal 9075 - Sao Paulo
S.P Brazil (1)

LCDR Emmanuel Gama de Almeida
Directoria de Hidrografia e Navegacao
ILHA Fiscal - Rio de Janerio
Guanabara - Brazil (1)

E. Paul McClain
ESC
ESSA
FOB 4
Washington, D. C. 20233 (1)